bioRχiv

Pearling Drives Mitochondrial DNA Nucleoid Distribution

Juan C. Landoni[1‡], Matthew D. Lycas[1], Josefa Macuada[1,2], Roméo Jaccard[1], Christopher J. Obara[3], Andrew S. Moore[3], Sheda Ben Nejma[1], David Hoffman[3], Jennifer Lippincott-Schwartz[3], Wallace Marshall[4], Gabriel Sturm[4], Suliana Manley[1‡]

[1] Institute of Physics, École Polytechnique Fédérale de Lausanne (EPFL), Lausanne, Switzerland.
[2] Faculty of Biological Sciences, Pontificia Universidad Católica de Chile, Santiago de Chile, Chile.
[3] Janelia Research Campus, Howard Hughes Medical Institute, Ashburn, USA.
[4] Department of Biochemistry and Biophysics, University of California, San Francisco, USA.
‡ Corresponding authors. Emails: juan.landoni@epfl.ch; suliana.manley@epfl.ch

Abstract

The regular distribution of mitochondrial DNA-containing nucleoids is essential for mitochondrial function and genome inheritance; however, the underlying mechanisms remain unknown. Our data reveal that mitochondria frequently undergo spontaneous and reversible pearling – a biophysical instability in which tubules undulate into regularly spaced beads. We discovered that pearling imposes a characteristic length scale, simultaneously mediating nucleoid disaggregation and establishing inter-nucleoid distancing with near-maximally achievable precision. Cristae invaginations play a dual role: lamellar cristae density determines pearling frequency and duration, and preserves the resulting nucleoid spacing after recovery. The distribution of mitochondrial genomes is thus fundamentally governed by the interplay between spontaneous pearling and cristae ultrastructure.

Introduction

Mitochondria carry their own independently replicating genome, mitochondrial DNA (mtDNA), which is considered a remnant of their endosymbiotic origins (*1*). In humans, mtDNA encodes 13 core subunits of the oxidative phosphorylation system, as well as RNAs required for their expression. Consequently, mtDNA integrity and copy number maintenance are critical for mitochondrial function and cellular health, with their disruption leading to a range of severe diseases (*2*). Each human cell contains hundreds of mtDNA copies (*3*), housed within the organelle's matrix and packaged by the transcription factor TFAM into nucleoids (*4*, *5*). Nucleoids are regularly spaced in yeast and human cells (*6*), and are locally confined by inner membrane cristae invaginations which act as diffusion barriers (*7*).

Regular spacing enables precise inheritance of mtDNA by daughter cells during division (*8*, *9*), and likely allows for well-distributed gene expression along the mitochondrion (*10*, *11*). However, no molecular machinery has thus far been identified to segregate nucleoids or maintain their regular distancing. While defects in mitochondrial dynamics can disrupt nucleoid homeostasis (*12*, *13*), mitochondria can maintain nucleoid distribution in the absence of fission and fusion in yeast (*9*, *14*) and upon removal of fission and tethering in human cells (*15*), indicating that the underlying mechanism remains to be discovered.

Our data indicate that the mitochondrial *pearling* instability— a shape transition from a tubule into beads-on-a-string—is a spontaneous, rapid, frequent and typically reversible event in eukaryotic

mitochondrial dynamics. Reminiscent of the Plateau-Rayleigh instability driven by competition between elasticity and surface tension (*16*, *17*), these simultaneously-occurring, regularly spaced constrictions have been reported anecdotally before (*18–20*) and were recently described as priming steps for mitochondrial fission (*21*, *22*). Here, we combine super-resolution microscopy approaches and the modulation of cristae morphology, fission and calcium dynamics to demonstrate the role of emergent *pearling* in redistributing mtDNA copies and establishing the long enigmatic regular distancing of nucleoids.

Mitochondrial pearling is a spontaneous and reversible biophysical instability.

Mitochondrial pearling has typically been investigated following its induction (*i.e.* by membrane rupture, calcium ionophore treatment or mitochondrial hyper-elongation), so we sought to observe its occurrence in steady-state conditions. Spontaneous pearling events occurred in untreated U2-OS cells (Fig 1A & S1A, Movie S1) with an incidence of ~1.3 events/cell/min under widefield fluorescence imaging, and emerged rapidly from one frame to the next (when imaging up to 100 frames-per-second). Pearling events often ended with a fission at one or more of the constrictions (Movie S1) and lasted 5-30 seconds, consistent with previous reports (*19*). The mean pearl diameter was 425 ± 86 nm (Fig. 1B, Fig. S1B), and the median number of pearls was five, although we observed strings of up to 34 pearls (Fig. S1A).

To investigate the finer ultrastructure of pearling, we turned to electron microscopy of U2-OS cells immobilized in a near-native state by high-pressure freezing. Following freeze-substitution and subsequent focused ion beam-scanning electron microscopy (FIB-SEM) (Fig. 1C, Fig. S1C), we observed that inner and outer mitochondrial membranes (IMM, OMM) can remain continuous during spontaneous pearling, leaving the matrix connected but tightly constricted. Our data presented a relatively low density of cristae, especially in pearled mitochondria (Fig. 1C), compared with other reports in HeLa cells (*23*, *24*). Live STED imaging of the IMM corroborated this observation, with lower cristae density in U2-OS cells than HeLa cells (Fig. S1D), and pearls frequently devoid of cristae signal (Fig. 1D). Pearl morphology was consistent between STED and EM images and using either matrix or OMM markers (Fig. S1B).

We observed that ~80% of events begin in contact with an ER tubule (Fig. 1E, Fig. S1E), consistent with previous reports of its role in triggering pearling (*21*, *22*). However, not every constriction appeared proximal to the ER (Fig. 1F), suggesting that the ER is not required at the site of all pearling constrictions for their stabilization.

Physically, a membrane tube can remain stable as long as its elastic resistance to deformation dominates over its membrane tension, which otherwise drives spherical shapes (*16*, *17*). The elasticity of a mitochondrion arises from its membranes and cristae folds, so we expected that modulating cristae density could modify pearling onset and stability. While most cristae perturbations disrupt mitochondrial homeostasis, removal of the mitochondrial contact site and cristae organizing system (MICOS) core subunit MIC10 in HeLa cells can deplete lamellar cristae with mild-to-negligible effects on respiratory chain assembly or network morphology (*25*). Depletion of MIC10 (siMIC10) in cristae-dense HeLa cells resulted in a striking increase in spontaneous pearling probability when compared to siRNA controls (Fig. 1G-H & S1F). In addition to frequent reversible events, persistent pearling events lasting longer than a minute or even beyond the entire 6-minute acquisition, were abundant in siMIC10 cells (Fig. 1I). This supports our model that disrupting lamellar cristae diminished the ability of mitochondria to elastically resist and recover from the instability, and thereby increased the prevalence of the pearled morphology.

To examine the potential effects of experimental conditions on pearling, we imaged cells using an array of labels (OMM- and matrix-targeted fluorescent proteins, vital stains), and microscopy techniques (widefield epi-fluorescence, instant structured illumination microscopy (iSIM), stimulated emission depletion (STED) microscopy, and phase contrast microscopy). Under all conditions, mitochondria displayed spontaneous and reversible pearling events (Fig. 1A, D-E, S1A).

Additionally, we detected pearling events across different mammalian cell types (COS-7, HeLa, primary fibroblasts), and the yeast *Saccharomyces cerevisiae* (Fig. S1A), indicating that spontaneous and reversible pearling is a physiological and evolutionarily conserved shape transformation in mitochondrial dynamics.

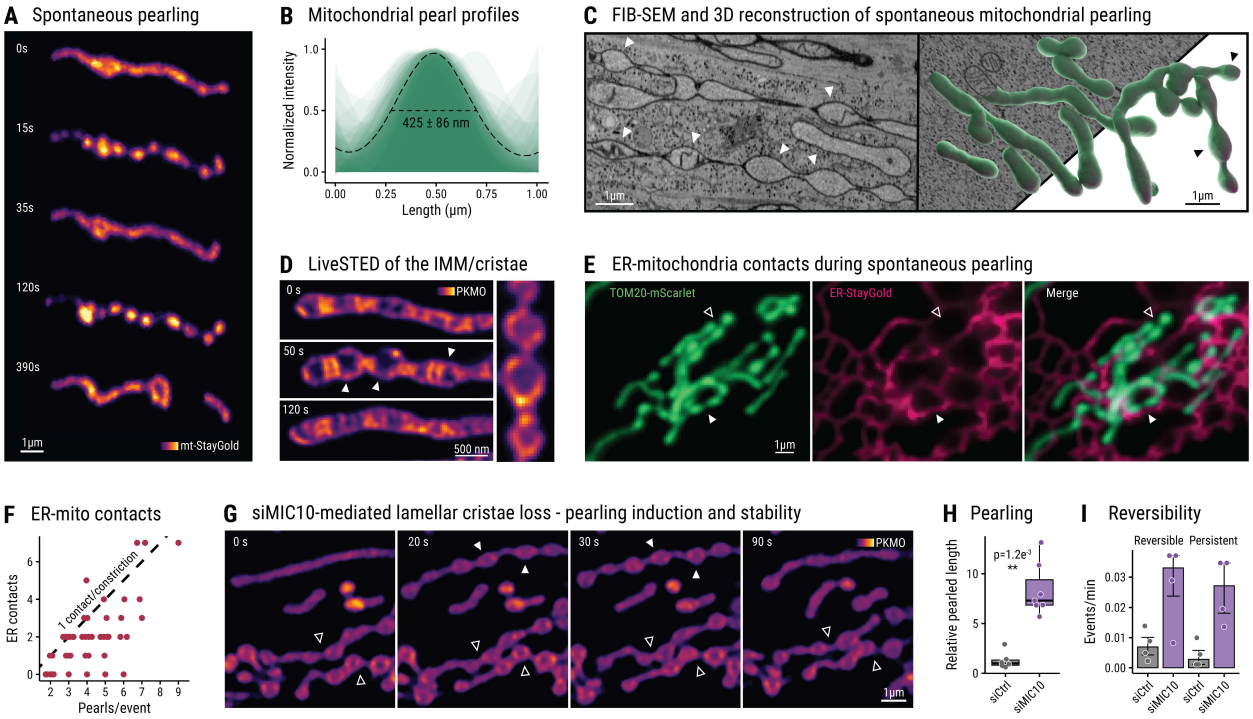

Fig. 1. Spontaneous mitochondrial pearling. (A) U2-OS cell mitochondrion (mt-StayGold) undergoing consecutive reversible pearling (15 s, 120 s), and fission (390 s) in iSIM. **(B)** Line profiles of 50 spontaneous pearls (mt-StayGold as in (A)), with the mean full-width half-max diameter. **(C)** FIB-SEM image and 3D reconstructions of mitochondria (select pearls, arrowheads). **(D)** Time-lapse and snapshot of PKMO-labeled IMM cristae during spontaneous pearling (arrowheads) in live STED microscopy. **(E)** OMM (TOM20-mScarlet, green) and endoplasmic reticulum (ER-StayGold, pink), highlighting pearling constrictions with (filled arrowhead) or without (empty arrowhead) mitochondria-ER proximity. **(F)** Number of ER-mitochondria contacts versus the number of pearls, from data as in (E). Each jittered point represents an independent pearling event; the dashed line represents one contact at every pearl constriction. **(G)** siRNA-mediated MIC10 silenced HeLa cells, highlighting rapidly reversible (filled arrowheads) or persistent (empty arrowheads) pearling events. AiryScan imaging of PKMO-stained mitochondria. **(H)** Pearling in siRNA control (n = 6) and siMIC10 (n = 7) cells as in (G): proportion of the total mitochondrial network length which pearls within 1 minute, normalized to median of controls **(I)** Mean reversible pearling event rate per minute per experiment (n = 4 independent experiments), defined by pearling completed within a minute or the end of acquisition time. Bar and box plots represent median ± IQR of the overlaid datapoints, p values from two-sided Wilcoxon test.

Pearling entrains mtDNA nucleoids.

As is characteristic of Rayleigh-Plateau-like instabilities, spontaneous mitochondrial pearling presents undulations of a characteristic wavelength, in this case a mean distance between pearls of 0.81±0.13 µm as measured by STED microscopy (Fig. 2A). This distance is nearly identical to the median spacing of mtDNA nucleoids we measure along 3D mitochondrial networks in U2-OS cells with light sheet microscopy (0.84±0.13 µm, Fig. 2B) and published values in yeast (*8*, *9*), which prompted us to investigate the relationship between pearling and nucleoids.

Dual-color STED imaging of nucleoids and IMM revealed nucleoids in regions devoid of cristae (Fig. S2A), consistent with previous reports (*23*, *26*). Most pearls contained a nucleoid, located near their center by both STED (Fig. 2C, Movie S2) and iSIM (Fig. 2D). Nonetheless, pearling morphology and dynamics were unchanged in the absence of nucleoid foci, both in control conditions (Fig. 2E, Fig. S2B) and following mtDNA depletion by ethidium bromide (Fig. 2F, Fig. S2C), indicating that nucleoids do not determine pearling onset or shape.

Instead, we speculated that pearling may directly impact nucleoid positioning. Using live iSIM, we assessed nucleoid organization before, during and after spontaneous pearling events. In contrast to their sometimes diffuse or irregular organization pre-pearling, nucleoids within pearls appeared as distinct puncta (Fig. 2G-H) with the regular spacing expected from population averages (Fig. 2I). We replicated these results using genetically encoded (mt-StayGold and TFAM-RFP) and dye-based probes (SYBR gold and MitoTracker Red FM), excluding possible effects of dye intercalation or protein overexpression. Thus, the onset of pearling can reshape and redistribute nucleoids, resulting in more discrete and regularly spaced foci.

To gather statistics on how pearling redistributes nucleoids, we measured the distances between neighboring nucleoids before, during, and after pearling in a larger dataset from widefield microscopy (Fig. 2J). Pearling-associated nucleoid spacing replicated the non-random spacing from light sheet data (Fig. 2B) and previous reports (*8*, *9*), peaking at 800-900 nm. Moreover, the onset of pearling leads to a narrower and more symmetrical distribution when compared to the pre-pearling conditions. Importantly, post-recovery to a native tubular shape, the distribution remains narrower (Fig. 2J), and the median distances between nucleoids are significantly smaller (Fig. 2K) compared with pre-pearling. Comparable measurements in *Saccharomyces cerevisiae* revealed a similar regularization during pearling, albeit at a larger distance than in mammalian cells (Fig. S2D).

Taken together, our data provide evidence that pearling establishes an emergent length scale, characteristic to the organelle, which dynamically entrains nucleoids and drives their distribution across the network (Movie S2).

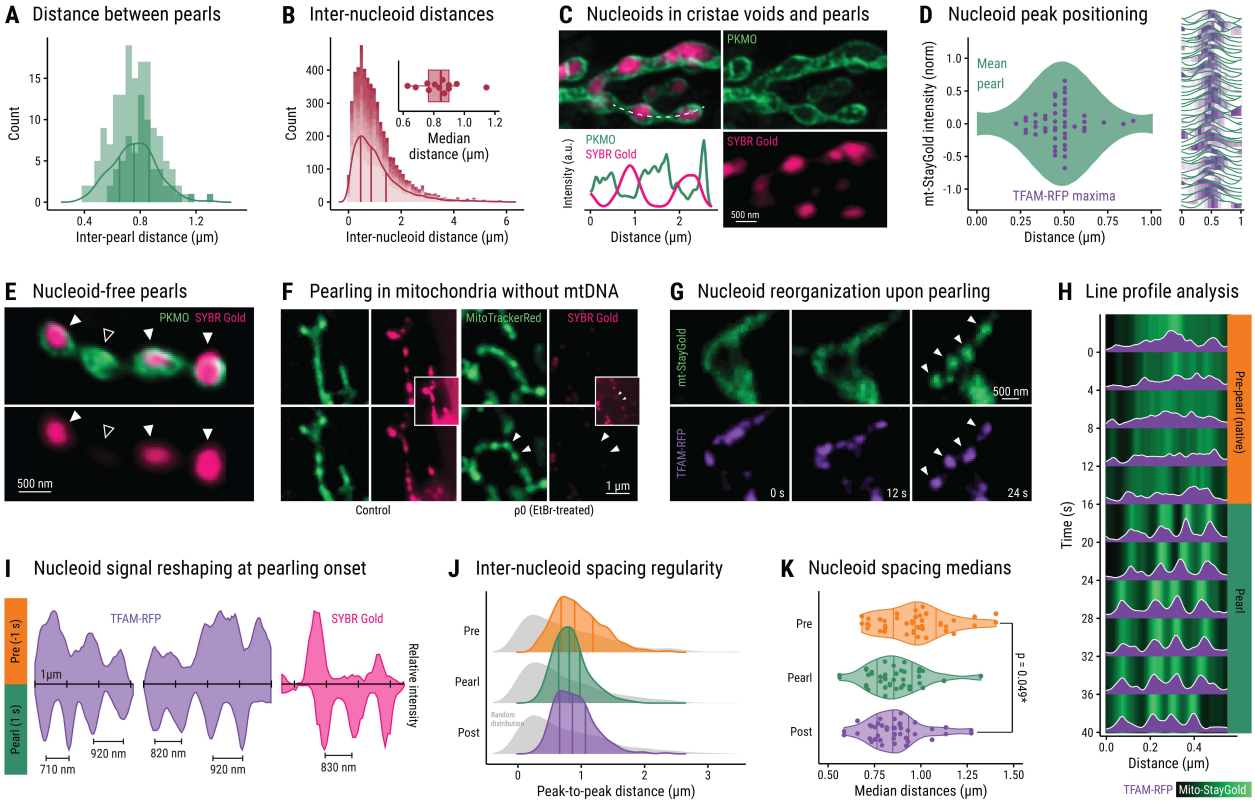

Fig. 2. Pearling-driven mtDNA redistribution. (A) Distribution of inter-pearl distances, as measured by iSIM and STED (dim and dark histograms respectively), overlaid with a density curve and vertical median and inter-quartile range lines (n = 87+63 inter-pearl distances). **(B)** Inter-nucleoid distance distribution along 3D light sheet images of mitochondria and nucleoids (PKMO and SYBR gold staining). Different cells are displayed as different shades in the stacked histogram, each cell's medians as inset (n = 5319 inter-nucleoid distances in 12 cells). **(C)** Live STED imaging of IMM (PKMO, green) and nucleoid (SYBR gold, pink). Line profile (bottom left) displaying relative intensities along the dashed line (representative from n = 4 independent experiments). Note: SYBR gold is not STED-compatible, nucleoids appear larger than their actual size. **(D)** Position of nucleoid maxima (TFAM-RFP, indigo) displayed relative to the average profile of a pearl (mt-StayGold, mirrored). On the right, individual pearl profiles with nucleoid intensity heatmap in indigo (n = 50 pearls). **(E)** Spontaneous pearling as in (C), with nucleoid-occupied (filled arrowheads) and a nucleoid-free pearl (empty arrowhead). **(F)** Spontaneous pearling captured in control and ethidium bromide-treated conditions (mtDNA-free mitochondria), n = 2 independent experiments. Saturated contrast insets to highlight the lack of SYBR gold signal. **(G-H)** Timelapse of spontaneous pearling as in (D), showing nucleoid (TFAM-RFP, indigo) signal condensation concomitant with mitochondrial (mt-StayGold, green) pearling onset (G), and corresponding kymograph and line profiles (H). **(I)** Normalized mtDNA intensity line profile examples, from TFAM-RFP (indigo) or SYBR gold (pink) signal immediately before and after pearling onset (mirrored). **(J-K)** Distribution of inter-nucleoid distances during pearling (pearl) and within 10s before (pre) and after (post) pearling onset (J), with modeled random distributions for each population (gray density curves), and median values per independent pearling event (K), n = 21 independent events with an average of 5.5 nucleoids and 15 timepoints each. All pearling depicted and quantified were captured spontaneously from live imaging of non-induced U2-OS cells. Lines in density and violin plots represent median and IQR of the distribution.

Pearling onset drives nucleoid disaggregation. Nucleoid intensity profiles revealed that foci became smaller and sharper following pearling onset. Indeed, the full-width half-maxima of nucleoid foci (TFAM-RFP, Fig. 3A) consistently decreased after pearling, trending towards the expected size for a single nucleoid imaged by widefield microscopy (377 ± 61 nm post-pearling). While nucleoid compaction could lead to smaller puncta, their typical ~100 nm size (*27*, *28*) is beyond the resolution achievable in these diffraction-limited systems. In contrast, the dispersion of clustered nucleoids may appear as a detectable size shift, segregating mtDNA copies as smaller nucleoids (Fig. 3B).

Indeed, we captured splitting events concomitant with pearling (Fig. 3C-E, Movie S2), resulting in the separation of a larger and typically brighter nucleoid focus into two smaller, dimmer, and more spherical foci. The stoichiometry of SYBR gold fluorescent intensity before and after splitting indicates the nearly equal separation of mtDNA material into the two resulting nucleoids (Fig. 3F). Interestingly, the splitting event is not always simultaneous with pearling onset (Fig. 3F), suggesting a slower separation process triggered by the shape transition (*29*).

As an alternative method to measure mtDNA content of pearls, we turned to whole-cell FIB-SEM correlated with volumetric cryoSIM of nucleoids (SYBR green, Fig. 3G). We segmented all nucleoids and measured their integrated fluorescence intensity. Nucleoids within pearled mitochondria presented lower SYBR green intensity than the population average (Fig. 3H), suggesting they contain fewer mtDNA copies. Furthermore, the distribution of integrated nucleoid intensities displayed several distinct peaks. We interpreted the lowest intensity peak as corresponding to nucleoids containing a single mtDNA copy, consistent with our data on splitting (Fig. 3F) and published data (*28*). While most nucleoids contain more than three times the mtDNA content of the smallest population, pearled mitochondria are more strongly enriched by nucleoids in quanta 1 and 2 (Fig. 3I-J).

With the observed 1.3 events/cell/min, we can estimate a lower bound on the number of pearling events of 2,262, or about 10,000 individual constrictions per 29 h U2-OS cell cycle when factoring in the average number of pearls per event. Using pearling probability data (mean percentage of 6-11% of total network length pearling within a minute in control conditions) and assuming all mitochondria are equally likely to pearl, every part of the network could pearl 10-20 times within a cell cycle. These rough approximations indicate that steady-state pearling frequencies are likely to be sufficient to disaggregate newly made mtDNA copies and distribute new nucleoids along the network.

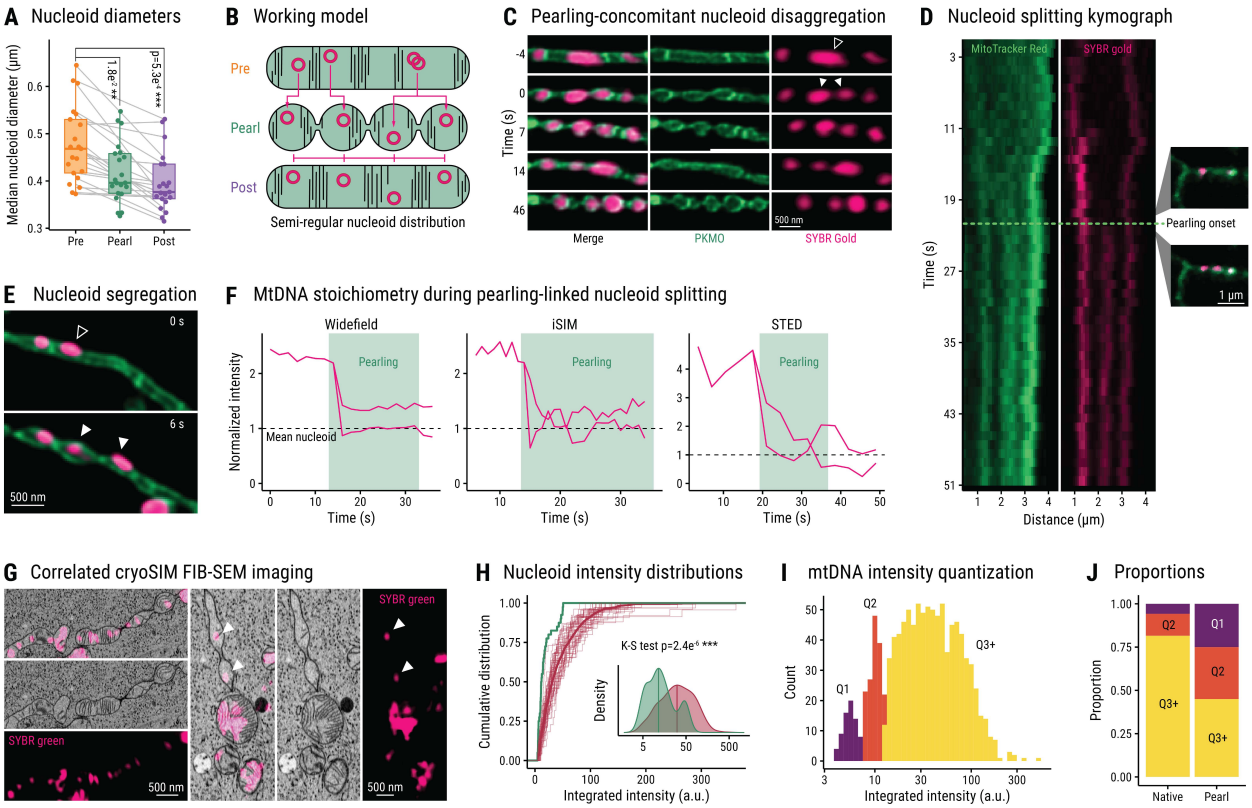

Fig. 3. Pearling mediates nucleoid disaggregation. (A) Median nucleoid diameter (FWHM of TFAM-RFP peak) per independent event during pearling (Pearl), as well as 10s before and after (Pre and Post). Boxplots represent median and IQR, p values from a two-sided Mann-Whitney test (n = 21 independent events with an average of 5.5 nucleoids and 15 timepoints each). **(B)** Working model of pearling-mediated nucleoid splitting and redistribution (matrix in green, nucleoids as pink circles, cristae represented as vertical black lines). **(C)** Live STED imaging of IMM (PKMO, green) and mtDNA (SYBR gold, pink) during spontaneous pearling. Arrowheads indicate nucleoid splitting (filled, pre; empty, post). **(D)** Kymograph of nucleoid disaggregation concomitant with pearling onset (dashed line), with snapshot insets 2 s before and after. **(E)** Nucleoid segregation event, as in (C). **(F)** Integrated intensity of nucleoids splitting during spontaneous pearling from different microscopes, normalized to the mean of neighboring non-splitting nucleoids (dashed line). Pearling duration shaded in green. **(G)** Representative images of spontaneous pearling FIB-SEM correlated with cryoSIM of nucleoids (SYBR green stain). **(H)** Cumulative distribution of nucleoid integrated intensity from data as (G), manually classified by their presence within pearled mitochondria in FIB-SEM (n = 1061+40 in native and pearled mitochondria respectively). Thick lines represent the whole population (p value from a Kolmogorov-Smirnov test), thin lines represent bootstrapping of 40-nucleoid groups, inset with $\log_{10}$ intensity distributions. **(I)** Histogram of nucleoid integrated intensity distribution ($\log_{10}$), with quantized populations in colors (Q2 peaks at twice the value of Q1, Q3+ is thrice Q1 and beyond). **(J)** Proportion of nucleoids classified according to their nucleoid intensity as in (I) in native or pearled mitochondria. All pearling depicted and quantified was captured spontaneously from non-induced U2-OS cells.

Nucleoid distance regularity is independent of mitochondrial fission

The inhibition of mitochondrial fission (typically by removal of its executor GTPase DRP1) reportedly increases pearling frequency and duration (*18*, *20*, *22*). Silencing of the DRP1 adaptor proteins mediating each type of mitochondrial fission (proliferative midzone fissions by siMFF and

damage-linked peripheral fissions by siFIS1) indeed led to hyperfused mitochondrial networks (Fig 4A) and increased pearling probability (Fig. 2B) already at 24h. We optimized treatment duration to achieve protein silencing (Fig. S2E-F) and an elongated network without severe pathology *e.g.* mtDNA clustering into mito-bulbs (*12*).

To obtain an unbiased view of the total distribution of inter-nucleoid distances, we segmented and skeletonized whole mitochondrial networks from volumetric iSIM immunofluorescent images (Methods), and quantified the distance between DNA peaks along these 3D skeletons. Then, using the total length and nucleoid number of each mitochondrion, we modeled two alternative nucleoid distributions: perfectly equidistant along each branch, and randomly distributed. As expected, the experimental distribution of distances was non-random, peaking very near to that of precise regularity (median of 789 ± 425 and 808 ± 312 nm respectively), albeit broader (Fig. 4C). We speculate that a limiting factor in achieving equidistant nucleoid spacing across all mitochondria in a cell could be the quantized nature of pearls and nucleoids themselves: mitochondrial lengths take on a continuous distribution, which leads to rounding errors when they are partitioned into discrete units.

The inhibition of fission did not affect the inter-nucleoid distance regularity, maintaining both the median value and variability coefficient (Fig. 4D, S2G). Similar to reports in yeast (*9*), this indicates that normal nucleoid distribution is independent of fission dynamics. Interestingly, the proximity of steady-state distancing to precise equidistance and the inability to further regularize it by increasing pearling occurrence suggests that physiological inter-nucleoid distributions are maintained near the limit of precision achievable via this mechanism.

Pearling-driven nucleoid distribution is triggered by intra-mitochondrial calcium and maintained by cristae confinement

To identify regulators of pearling-driven nucleoid redistribution, we manipulated pearling by additional approaches. Ionomycin can induce simultaneous pearling across the entire mitochondrial network (*21*, *22*), typically within 15-30 seconds of addition (Fig. 4E). This allowed us to obtain dynamic information of large-scale effects from a controlled trigger. The widespread induction of pearling consistently led to a reduction in cell-wide mean distances and regularization of the three-dimensional inter-nucleoid distance distribution compared to pre-treatment (Fig. 4F), supporting a causal relationship between network pearling and nucleoid distribution.

Consistent with the role of calcium in triggering pearling, siRNA-mediated depletion of the mitochondrial calcium uniporter (siMCU) decreases the probability of pearling (Fig. 4G, S2H) with little consequence on mitochondrial morphology (*22*). Furthermore, while fragments of the network presented normal nucleoid populations, we consistently observed enlarged and elongated nucleoids (over 2 µm long), hereby named 'nucleotes' (/*nu.kleˈo.tes*/), along with long stretches of nucleoid-free mitochondria (Fig. 4H). Nucleotes were typically stable during the ~1.5 min acquisition; undergoing apparent movement and bending from mitochondrial branching rarely resulted in their disaggregation. The disruption in nucleoid morphology and coverage in pearling-deficient siMCU cells supports the importance of intra-mitochondrial calcium and resultant pearling in nucleoid segregation.

In wild-type cells, nucleoids typically resided in cristae voids (Fig. S2A). In live STED, spontaneous pearls devoid of nucleoids frequently presented high cristae signal, potentially sterically excluding a nucleoid from that position (Fig. S2B). Thus, we sought to dissect the role of cristae on nucleoid distribution, taking advantage of siMIC10 as a model for lamellar cristae loss and increased pearling probability and stability (Fig. 1H-I). Most persistent pearls contained a nucleoid focus (Fig. 4I), and we observed nucleoid splitting and redistribution concomitant with reversible pearling onset (Fig. 4J-K), similar to steady-state conditions. Surprisingly, siMIC10 mitochondria frequently contained nucleotes up to 6 µm long and stretches of nucleoid-free mitochondria, morphologically similar to those in siMCU cells (Fig. 4L-M). Nucleote-containing mitochondria were particularly devoid of lamellar cristae (Fig. 4M).

Despite their fused appearance, pearling in siMIC10 cells readily separated nucleotes into

smaller foci (Fig. 4L-M), a phenotype replicated in a stable MIC10-KO cell line (Fig. 4M) (*25*). However, nucleotes divided by pearling in MIC10 deficient cells tend to rapidly re-merge, in contrast to wild-type cells where post-pearling mitochondrial tubules preserve nucleoid separation. This indicates that lamellar cristae integrity is required to retain inter-nucleoid distancing post-pearling, and that either the inability to pearl or to constrain nucleoid motion can independently cause nucleoid clustering and defective mtDNA coverage (Fig. 4N).

Taken together, our data supports a model wherein nucleoid disaggregation and distancing is independent of fission, and mechanistically driven by intra-mitochondrial calcium-triggered pearling. Furthermore, it emphasizes the critical importance of lamellar cristae integrity for the resistance to and recovery from pearling, as well as to maintain the established nucleoid separation.

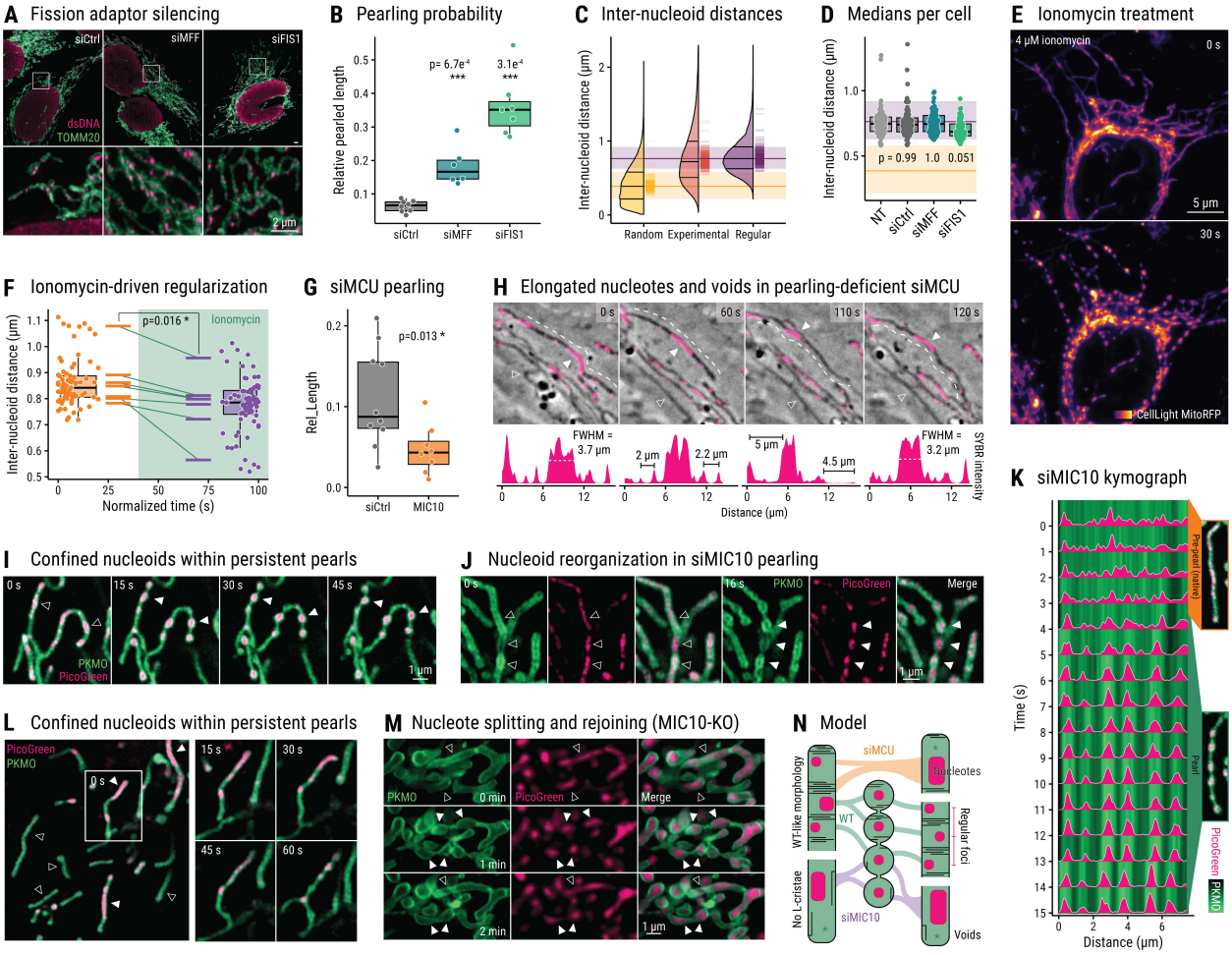

Fig. 4. Modulating pearling affects nucleoid distribution. (A) Volumetric immunofluorescence images of mitochondria and double-stranded DNA (TOM20 and dsDNA antibodies, max intensity projection), for control or silencing either MFF or FIS1 (n = 4 independent experiments). **(B)** Proportion of the total mitochondrial network undergoing pearling at least once within 1 minute (n = 8+6+7 cells). p values from a two-sided Wilcoxon test. **(C)** Distribution of 3D inter-nucleoid distances pooled among siMFF and siFIS1 experiments (Experimental), along with models (Random and Regular). Horizontal bars represent median and IQR, and barcode plot depicts median values per cell (n =72953 nucleoids across 453 cells, 2 independent experiments). **(D)** Median inter-nucleoid distance per cell in control or fission-deficient cells.

Horizontal shaded lines indicate median and IQR of random and regular distribution models as in (C), p values from an ANOVA/Tukey's HSD test against non-treated cells (n = 87+69+71+60 cells across 2 independent experiments). **(E)** Maximum intensity projection of a U2-OS cell mitochondrial network undergoing ionomycin-induced pearling (live light sheet imaging) (n = 12 independent experiments). **(F)** 3D inter-nucleoid distances before and during ionomycin-induced pearling. Points indicate median inter-nucleoid distance over time (centered around pearling onset), summarized by the boxplots, barcode plots represent the median value per independent experiment, p value from a paired two-sided Student's t-test (n = 12 independent experiments). **(G)** Proportion of the total mitochondrial network undergoing pearling at least once within 1 minute in control and MCU-silenced cells (n = 10+8 cells). **(H)** Timelapse of mitochondrial and nucleoid dynamics (dark tubules in phase-contrast and SYBR gold in pink, respectively) in MCU-deficient cells (n = 15 control + 18 siMCU cells, across 2 independent experiments). A nucleote (filled arrowheads) and a nucleoid-free mitochondrial stretch (empty arrowheads) are indicated. Bottom row displays the intensity line profiles of SYBR gold fluorescence along the mitochondrion (dashed line, displaced for clarity), with key measures exemplified (nucleote sizes as FWHM, larger inter-nucleoid distances, long nucleoid voids). **(I)** Persistent spontaneous pearling event in siMIC10 HeLa cell (n = 86 control + 91 siMIC10 cells, from 4 independent experiments). **(J)** Reversible pearling event as in (I), highlighting nucleoid organization before (empty arrowheads) and after (filled arrowheads) pearling onset. **(K)** Kymograph of a spontaneous siMIC10 pearling event, mitochondrial (PKMO) signal overlaid with line profile of mtDNA (PicoGreen), pre- and pearling periods indicated with snapshot insets. **(L)** Overview of siMIC10 nucleoid defects: nucleotes (filled arrowheads) and nucleoid-free mitochondria stretches (empty arrowheads). Inset: timelapse of pearling-mediated nucleote disaggregation (n = 86 control + 91 siMIC10 cells, from 4 independent experiments). **(M)** STED imaging of cristae (PKMO) and nucleoids (PicoGreen) in MIC10-KO HeLa cells, highlighting nucleotes (empty arrowheads) separated into nucleoid-like foci upon pearling (filled arrowheads) and rejoined into nucleotes following recovery (n = 2 independent experiments). **(N)** Graphical model of modulation effects: WT-like mitochondria (green, including siCtrl, siMFF and siFIS1) can undergo pearling then recover, and thus disaggregate enlarged nucleoids and establish regular distancing. The inability to pearl (siMCU, orange) or the lack of lamellar cristae to maintain pearling-mediated separation (siMIC10, indigo) leads to nucleoid aggregation into nucleotes and nucleoid voids (*). Box plots represent median ± IQR of the overlaid datapoints. DsDNA = double-stranded DNA, NT = non-treated, si- = siRNA-silenced, siCtrl = siRNA non-targeting control.

Discussion

Multinucleated systems typically exhibit spatial control of their genetic material. Whether in the syncytium of a developing organism or the interior of a filamentous bacterium, genetic material is generally spaced at regular intervals. In mitochondria, regular spacing ensures coverage, accurate inheritance and quality control (*8*, *30*, *31*). Furthermore, mitochondrial function relies on local gene expression, due to the limited sphere of influence of each nucleoid arising from locally constrained protein diffusion (*10*, *11*) and the need for rapid responses to localized stress in the organelle (*32*). Canonical fission and fusion dynamics, fission-linked mtDNA segregation (*33*, *34*) and nucleoid trafficking mediated by the membrane protein ATAD3 and dynamic tubulation (*15*, *35*) play important roles in nucleoid homeostasis and fine-tuning positioning. However, non-random distancing and inheritance can be maintained both in the absence of fission and fusion (*9*) and upon the combined removal of ATAD3 and DRP1 (*15*). Instead, pearling manifests as spontaneous and reversible undulations across the network, which sterically constrain nucleoid positions, establishing a consistent length scale without requiring active transport. Pearling can be triggered by intra-mitochondrial calcium (*21*, *22*) and result in fission, perhaps by creating pre-constrictions where the fission machinery can assemble (*36*). As such, our model reconciles the fission-independence of nucleoid distribution with the existing paradigms of calcium-induced pre-

constriction (*21*, *22*) and fission-linked mtDNA replication (*33*, *34*).

Modulating most cristae-organizing proteins can disrupt or fragment mitochondrial networks (*25*, *37*); in contrast, removing MIC10 allowed us to specifically assess the structural role of lamellar cristae in otherwise healthy elongated mitochondrial networks (*25*). Our data highlights the multifaceted role of lamellar cristae ultrastructure in mitochondrial and nucleoid homeostasis. On one hand, cristae maintain the elasticity of the mitochondrion, defining both the resistance to and recovery from pearling. On the other, the integrity of lamellar cristae is critical to confine nucleoids following their segregation and recovery from pearling. Pearling and lamellar cristae thus have a synergistic and essential role in ensuring mtDNA homeostasis. Along with the close relationship between cristae density, metabolic status and respiratory efficiency (*38*), this feedback brings forth the intriguing possibility of pearling frequency responding to metabolic demands, mitochondrial health and mtDNA integrity. Nucleotes additionally join the list of disrupted nucleoid morphologies, alongside fission-deficient mito-bulbs and enlarged nucleoids caused by replisome defects (*12*, *39*, *40*).

Some of our measurements use rapid high-resolution imaging to capture spontaneous pearling, and thus are limited by its phototoxicity. To address this, we tested many combinations of imaging and labeling paradigms (Fig. S1A), all the way to label-free phase-contrast microscopy, orders of magnitude gentler than fluorescence. Our study was also constrained to perturbations targeting specific machinery (i.e. fission adaptors, cristae organizing proteins) without disrupting the tubular network due to their inherent pleiotropy (*41*). To address this, we applied treatments for minimal durations (down to 60 seconds of ionomycin, 24-hour siRNA).

The evolution of mitochondria from a prokaryotic endosymbiont into the multifaceted organelle it is today has been largely reductive (*32*), with the exceptional innovation of an elongated and highly dynamic network (*42*). This network allows for plasticity, genetic complementation and access to the cell's farthest corners. However, in the absence of a cell wall, such tubular shapes under tension are subject to physical laws which can drive shape changes (*16*, *43*, *44*). The pearling instability arises from the competition between elastic resistance and interfacial tension, does not require energy consumption, and is reported in a wide variety of biological systems – long neuronal processes (*43*), infected endosomal networks (*45*), and the ER (*46*). Bacteria, free-living ancestors of mitochondria, can leverage outer membrane pearling for substrate sensing and binding, vesicle generation, and DNA transfer (*47–50*). Our findings indicate that the localized occurrence of pearling is both common and readily reversible in physiological conditions and is harnessed by the mitochondrial network to ensure the regular distribution of its genome.

References

1. L. Sagan, On the origin of mitosing cells. *J. Theor. Biol.* **14**, 255–274 (1967).

2. G. S. Gorman, P. F. Chinnery, S. DiMauro, M. Hirano, Y. Koga, R. McFarland, A. Suomalainen, D. R. Thorburn, M. Zeviani, D. M. Turnbull, Mitochondrial diseases. *Nat. Rev. Dis. Primer* **2**, 16080 (2016).

3. F. Legros, F. Malka, P. Frachon, A. Lombès, M. Rojo, Organization and dynamics of human mitochondrial DNA. *J. Cell Sci.* **117**, 2653–2662 (2004).

4. M. M. K. Nass, S. Nass, Intramitochondrial Fibers With DNA Characteristics. *J. Cell Biol.* **19**, 593–611 (1963).

5. J. N. Spelbrink, F. Y. Li, V. Tiranti, K. Nikali, Q. P. Yuan, M. Tariq, S. Wanrooij, N. Garrido, G. Comi, L. Morandi, L. Santoro, A. Toscano, G. M. Fabrizi, H. Somer, R. Croxen, D. Beeson, J. Poulton, A. Suomalainen, H. T. Jacobs, M. Zeviani, C. Larsson, Human mitochondrial DNA deletions associated with mutations in the gene encoding Twinkle, a phage T7 gene 4-like protein localized in mitochondria. *Nat. Genet.* **28**, 223–231 (2001).

6. F. J. Iborra, H. Kimura, P. R. Cook, The functional organization of mitochondrial genomes in human cells. *BMC Biol.* **2**, 1–14 (2004).

7. C. E. J. Dieteren, S. C. A. M. Gielen, L. G. J. Nijtmans, J. A. M. Smeitink, H. G. Swarts, R. Brock, P. H. G. M. Willems, W. J. H. Koopman, Solute diffusion is hindered in the mitochondrial matrix. *Proc. Natl. Acad. Sci.* **108**, 8657–8662 (2011).

8. R. Jajoo, Y. Jung, D. Huh, M. P. Viana, S. M. Rafelski, M. Springer, J. Paulsson, Accurate concentration control of mitochondria and nucleoids. *Science* **351**, 169–172 (2016).

9. C. Osman, T. R. Noriega, V. Okreglak, J. C. Fung, P. Walter, Integrity of the yeast mitochondrial genome, but not its distribution and inheritance, relies on mitochondrial fission and fusion. *Proc. Natl. Acad. Sci.* **112**, E947–E956 (2015).

10. K. B. Busch, A. Kowald, J. N. Spelbrink, Quality matters: how does mitochondrial network dynamics and quality control impact on mtDNA integrity? *Philos. Trans. R. Soc. B Biol. Sci.* **369**, 20130442 (2014).

11. C. Jakubke, R. Roussou, A. Maiser, C. Schug, F. Thoma, D. Bunk, D. Hörl, H. Leonhardt, P. Walter, T. Klecker, C. Osman, Cristae-dependent quality control of the mitochondrial genome. *Sci. Adv.* **7**, eabi8886 (2021).

12. R. Ban-Ishihara, T. Ishihara, N. Sasaki, K. Mihara, N. Ishihara, Dynamics of nucleoid structure regulated by mitochondrial fission contributes to cristae reformation and release of cytochrome c. *Proc. Natl. Acad. Sci.* **110**, 11863–11868 (2013).

13. R. Quintana-Cabrera, L. Scorrano, Determinants and outcomes of mitochondrial dynamics. *Mol. Cell* **83**, 857–876 (2023).

14. J. Tauber, A. Dlasková, J. Šantorová, K. Smolková, L. Alán, T. Špaček, L. Plecitá-Hlavatá, M. Jabůrek, P. Ježek, Distribution of mitochondrial nucleoids upon mitochondrial network fragmentation and network reintegration in HEPG2 cells. *Int. J. Biochem. Cell Biol.* **45**, 593–603 (2013).

15. T. Ishihara, R. Ban-Ishihara, A. Ota, N. Ishihara, Mitochondrial nucleoid trafficking regulated by the inner-membrane AAA-ATPase ATAD3A modulates respiratory complex formation. *Proc. Natl. Acad. Sci.* **119**, e2210730119 (2022).

16. G. Boedec, M. Jaeger, M. Leonetti, Pearling instability of a cylindrical vesicle. *J. Fluid Mech.* **743**, 262–279 (2014).

17. D. Gonzalez-Rodriguez, S. Sart, A. Babataheri, D. Tareste, A. I. Barakat, C. Clanet, J. Husson, Elastocapillary Instability in Mitochondrial Fission. *Phys. Rev. Lett.* **115**, 088102 (2015).

18. A. M. Labrousse, M. D. Zappaterra, D. A. Rube, A. M. V. der Bliek, C. elegans dynamin-related protein DRP-1 controls severing of the mitochondrial outer membrane. *Mol. Cell* **4**, 815–826 (1999).

19. H. Lee, Y. Yoon, Transient Contraction of Mitochondria Induces Depolarization through the Inner Membrane Dynamin OPA1 Protein*. *J. Biol. Chem.* **289**, 11862–11872 (2014).

20. A. Legesse-Miller, R. H. Massol, T. Kirchhausen, Constriction and Dnm1p recruitment are distinct processes in mitochondrial fission. *Mol. Biol. Cell* **14**, 1953–1963 (2003).

21. R. Chakrabarti, W.-K. Ji, R. V. Stan, J. de Juan Sanz, T. A. Ryan, H. N. Higgs, INF2-mediated actin polymerization at the ER stimulates mitochondrial calcium uptake, inner membrane constriction, and division. *J. Cell Biol.* **217**, 251–268 (2017).

22. B. Cho, H. M. Cho, Y. Jo, H. D. Kim, M. Song, C. Moon, H. Kim, K. Kim, H. Sesaki, I. J. Rhyu, H. Kim, W. Sun, Constriction of the mitochondrial inner compartment is a priming event for mitochondrial division. *Nat. Commun.* **8** (2017).

23. T. Stephan, A. Roesch, D. Riedel, S. Jakobs, Live-cell STED nanoscopy of mitochondrial cristae. *Sci. Rep.* **9**, 12419 (2019).

24. C. Wang, M. Taki, Y. Sato, Y. Tamura, H. Yaginuma, Y. Okada, S. Yamaguchi, A photostable fluorescent marker for the superresolution live imaging of the dynamic structure of the mitochondrial cristae. *Proc. Natl. Acad. Sci.* **116**, 15817–15822 (2019).

25. T. Stephan, C. Brüser, M. Deckers, A. M. Steyer, F. Balzarotti, M. Barbot, T. S. Behr, G. Heim, W. Hübner, P. Ilgen, F. Lange, D. Pacheu-Grau, J. K. Pape, S. Stoldt, T. Huser, S. W. Hell, W. Möbius, P. Rehling, D. Riedel, S. Jakobs, MICOS assembly controls mitochondrial inner membrane remodeling and crista junction redistribution to mediate cristae formation. *EMBO J.* **39**, e104105 (2020).

26. B. G. Kopek, G. Shtengel, C. S. Xu, D. A. Clayton, H. F. Hess, Correlative 3D superresolution fluorescence and electron microscopy reveal the relationship of mitochondrial nucleoids to membranes. *Proc. Natl. Acad. Sci.* **109**, 6136–6141 (2012).

27. T. A. Brown, A. N. Tkachuk, G. Shtengel, B. G. Kopek, D. F. Bogenhagen, H. F. Hess, D. A. Clayton, Superresolution Fluorescence Imaging of Mitochondrial Nucleoids Reveals Their Spatial Range, Limits, and Membrane Interaction. *Mol. Cell. Biol.* **31**, 4994–5010 (2011).

28. C. Kukat, C. A. Wurm, H. Spåhr, M. Falkenberg, N. G. Larsson, S. Jakobs, Super-resolution microscopy reveals that mammalian mitochondrial nucleoids have a uniform size and frequently contain a single copy of mtDNA. *Proc. Natl. Acad. Sci. U. S. A.* **108**, 13534–13539 (2011).

29. S. Jun, A. Wright, Entropy as the driver of chromosome segregation. *Nat. Rev. Microbiol.* **8**, 600–607 (2010).

30. N. Garrido, L. Griparic, E. Jokitalo, J. Wartiovaara, A. M. V. der Bliek, J. N. Spelbrink, Composition and dynamics of human mitochondrial nucleoids. *Mol. Biol. Cell* **14**, 1583–1596 (2003).

31. T. Kleele, T. Rey, J. Winter, S. Zaganelli, D. Mahecic, H. P. Lambert, F. P. Ruberto, M. Nemir, T. Wai, T. Pedrazzini, S. Manley, Distinct fission signatures predict mitochondrial degradation or biogenesis. *Nature* **593**, 435–439 (2021).

32. N. Lane, W. Martin, The energetics of genome complexity. *Nature* **467**, 929–934 (2010).

33. S. C. Lewis, L. F. Uchiyama, J. Nunnari, ER-mitochondria contacts couple mtDNA synthesis with Mitochondrial division in human cells. *Science* **353**, aaf5549 (2016).

34. A. Murley, L. L. Lackner, C. Osman, M. West, G. K. Voeltz, P. Walter, J. Nunnari, ER-associated mitochondrial division links the distribution of mitochondria and mitochondrial DNA in yeast. *eLife* **2013** (2013).

35. J. Qin, Y. Guo, B. Xue, P. Shi, Y. Chen, Q.-P. Su, H. Hao, S. Zhao, C. Wu, L. Yu, D. Li, Y. Sun, ER-mitochondria contacts promote mtDNA nucleoids active transportation via mitochondrial dynamic tubulation. *Nat. Commun.* **11**, 4471 (2020).

36. J. E. Lee, L. M. Westrate, H. Wu, C. Page, G. K. Voeltz, Multiple dynamin family members collaborate to drive mitochondrial division. *Nature* **540**, 139–143 (2016).

37. M. Y. Fry, P. P. Navarro, P. Hakim, V. Y. Ananda, X. Qin, J. C. Landoni, S. Rath, Z. Inde, C. M. Lugo, B. E. Luce, Y. Ge, J. L. McDonald, I. Ali, L. L. Ha, B. P. Kleinstiver, D. C. Chan, K. A. Sarosiek, L. H. Chao, In situ architecture of Opa1-dependent mitochondrial cristae remodeling. *EMBO J.*, 1–23 (2024).

38. C. F. Bennett, P. Latorre-Muro, P. Puigserver, Mechanisms of mitochondrial respiratory adaptation. *Nat. Rev. Mol. Cell Biol.* **23**, 817–835 (2022).

39. E. Ylikallio, H. Tyynismaa, H. Tsutsui, T. Ide, A. Suomalainen, High mitochondrial DNA copy number has detrimental effects in mice. *Hum. Mol. Genet.* **19**, 2695–2705 (2010).

40. J. C. Landoni, S. Erkul, T. Laalo, S. Goffart, R. Kivelä, K. Skube, A. I. Nieminen, S. A. Wickström, J. Stewart, A. Suomalainen, Overactive mitochondrial DNA replication disrupts perinatal cardiac maturation. *Nat. Commun.* **15**, 8066 (2024).

41. L.-C. Tábara, M. Segawa, J. Prudent, Molecular mechanisms of mitochondrial dynamics. *Nat. Rev. Mol. Cell Biol.*, doi: 10.1038/s41580-024-00785-1 (2024).

42. J. C. Landoni, T. Kleele, J. Winter, W. Stepp, S. Manley, Mitochondrial Structure, Dynamics, and Physiology: Light Microscopy to Disentangle the Network. doi: 10.1146/annurev-cellbio-111822-114733 (2024).

43. R. Bar-Ziv, T. Tlusty, E. Moses, S. A. Safran, A. Bershadsky, Pearling in cells: A clue to understanding cell shape. *Proc. Natl. Acad. Sci.* **96**, 10140–10145 (1999).

44. R. Bar-Ziv, E. Moses, Instability and “Pearling” States Produced in Tubular Membranes by Competition of Curvature and Tension. *Phys. Rev. Lett.* **73**, 1392–1395 (1994).

45. Y. Gao, C. Spahn, M. Heilemann, L. J. Kenney, The Pearling Transition Provides Evidence of Force-Driven Endosomal Tubulation during Salmonella Infection. *mBio* **9**, e01083-18 (2018).

46. C. J. Obara, A. S. Moore, J. Lippincott-Schwartz, Structural Diversity within the Endoplasmic Reticulum—From the Microscale to the Nanoscale. *Cold Spring Harb. Perspect. Biol.* **15**, a041259 (2023).

47. A. Dürwald, M.-K. Zühlke, R. Schlüter, R. Gebbe, D. Bartosik, F. Unfried, D. Becher, T. Schweder, Reaching out in anticipation: bacterial membrane extensions represent a permanent investment in polysaccharide sensing and utilization. *Environ. Microbiol.* **23**, 3149–3163 (2021).

48. T. Fischer, M. Schorb, G. Reintjes, A. Kolovou, R. Santarella-Mellwig, S. Markert, E. Rhiel, S. Littmann, D. Becher, T. Schweder, J. Harder, Biopearling of Interconnected Outer Membrane Vesicle Chains by a Marine Flavobacterium. *Appl. Environ. Microbiol.* **85**, e00829-19 (2019).

49. M. Kaplan, G. Chreifi, L. A. Metskas, J. Liedtke, C. R. Wood, C. M. Oikonomou, W. J. Nicolas, P. Subramanian, L. A. Zacharoff, Y. Wang, Y.-W. Chang, M. Beeby, M. J. Dobro, Y. Zhu, M. J. McBride, A. Briegel, C. L. Shaffer, G. J. Jensen, In situ imaging of bacterial outer membrane projections and associated protein complexes using electron cryo-tomography. *eLife* **10**, e73099 (2021).

50. C. Pérez-Cruz, O. Carrión, L. Delgado, G. Martinez, C. López-Iglesias, E. Mercade, New Type of Outer Membrane Vesicle Produced by the Gram-Negative Bacterium Shewanella vesiculosa M7T: Implications for DNA Content. *Appl. Environ. Microbiol.* **79**, 1874–1881 (2013).

51. D. Mahecic, D. Gambarotto, K. M. Douglass, D. Fortun, N. Banterle, K. A. Ibrahim, M. Le Guennec, P. Gönczy, V. Hamel, P. Guichard, S. Manley, Homogeneous multifocal excitation for high-throughput super-resolution imaging. *Nat. Methods* **17**, 726–733 (2020).

52. E. Czech, B. A. Aksoy, P. Aksoy, J. Hammerbacher, Cytokit: a single-cell analysis toolkit for high dimensional fluorescent microscopy imaging. *BMC Bioinformatics* **20**, 448 (2019).

53. Alfred Millett-Sikking, Andrew York, High NA single-objective light-sheet. doi: 10.5281/ZENODO.3376243 (2019).

54. D. P. Hoffman, G. Shtengel, C. S. Xu, K. R. Campbell, M. Freeman, L. Wang, D. E. Milkie, H. A. Pasolli, N. Iyer, J. A. Bogovic, D. R. Stabley, A. Shirinifard, S. Pang, D. Peale, K. Schaefer, W. Pomp, C.-L. Chang, J. Lippincott-Schwartz, T. Kirchhausen, D. J. Solecki, E. Betzig, H. F. Hess, Correlative three-dimensional super-resolution and block-face electron microscopy of whole vitreously frozen cells. *Science* **367**, eaaz5357 (2020).

55. C. Buser, P. Walther, Freeze-substitution: the addition of water to polar solvents enhances the retention of structure and acts at temperatures around –60°C. *J. Microsc.* **230**, 268–277 (2008).

56. C. S. Xu, K. J. Hayworth, Z. Lu, P. Grob, A. M. Hassan, J. G. García-Cerdán, K. K. Niyogi, E. Nogales, R. J. Weinberg, H. F. Hess, Enhanced FIB-SEM systems for large-volume 3D imaging. *eLife* **6**, e25916 (2017).

57. J. A. Bogovic, P. Hanslovsky, A. Wong, S. Saalfeld, "Robust registration of calcium images by learned contrast synthesis" in *2016 IEEE 13th International Symposium on Biomedical Imaging (ISBI)* (IEEE, Prague, Czech Republic, 2016; http://ieeexplore.ieee.org/document/7493463/), pp. 1123–1126.

58. D. R. Stirling, M. J. Swain-Bowden, A. M. Lucas, A. E. Carpenter, B. A. Cimini, A. Goodman, CellProfiler 4: improvements in speed, utility and usability. *BMC Bioinformatics* **22**, 433 (2021).

59. A. E. Y. T. Lefebvre, G. Sturm, T.-Y. Lin, E. Stoops, M. P. Lopez, B. Kaufmann-Malaga, K. Hake, Nellie: Automated organelle segmentation, tracking, and hierarchical feature extraction in 2D/3D live-cell microscopy. arXiv arXiv:2403.13214 [Preprint] (2024). https://doi.org/10.48550/arXiv.2403.13214.

60. F. Aymanns, E. Andò, V. Uhlmann, SplineBox (2024). https://doi.org/10.5281/zenodo.13358354.

61. M. C. Harwig, M. P. Viana, J. M. Egner, J. J. Harwig, M. E. Widlansky, S. M. Rafelski, R. B. Hill, Methods for imaging mammalian mitochondrial morphology: a prospective on MitoGraph. *Anal. Biochem.* **552**, 81–99 (2018).

Acknowledgements

The authors wish to thank Hélène Perreten, Kyle Douglass, Willi Stepp, Giorgio Tortarolo, Julius Winter, Christian Zimmerli, Austin Lefebvre, Quentin Kohler, Carolin Klose, and Asa Kalish for their invaluable technical assistance and inspiring discussions. We thank the EPFL Center for Imaging (especially Florian Aymanns) for their support with image analysis. The EPFL Laboratory of Experimental Biophysics (LEB), the MBL Physiology Course and the HFSP "MitoManiacs" are also thanked for providing an enriching environment for discovery in fundamental science. We thank Stefan Jakobs and Till Stephan for kindly sharing their HeLa cell models, and Gleb Shtengel, Harald Hess, Eric Betzig, and Shan Xu for their contributions in developing the cryo-SIM FIB-SEM technique.

Funding

Human Frontier of Science Program (HSFP, RGP0038/2021) (S.M., W.M.)

European Research Council (CoG 819823, Piko) (S.M.)

The Swiss National Science Foundation (SNSF, 10268) (S.M.)

The Swiss State Secretariat for Education, Research and Innovation (SERI) CLS-HSG Research Partnership (SCR0835124) (S.M.)

Agencia Nacional de Investigación y Desarrollo de Chile (Ph.D. Fellowship 21211363) (J.M.)

Swiss Government Excellence Research Fellowship (FCS 2023.0400) (J.M.)

Author contributions

Conceptualization: J.C.L., S.M.

Methodology: J.C.L., M.D.L., J.M., G.S., C.J.O., A.S.M., S.B.N., D.H.

Investigation: J.C.L., M.D.L., J.M., G.S., R.J., C.J.O., A.S.M., S.B.N.

Visualization: J.C.L.

Writing – original draft: J.C.L., S.M.

Writing – review and editing: All authors

Project administration: S.M., J.C.L.

Funding acquisition: S.M.

Competing interests:

The authors declare that they have no competing interests

Supplementary Materials

Materials and Methods

Figs. S1 and S3

Movies S1 to S3

Supplementary Materials for

Pearling Drives Mitochondrial DNA Nucleoid Distribution

Juan C Landoni, Matthew D Lycas, Josefa Macuada, Roméo Jaccard, Christopher J Obara, Andrew S Moore, Sheda Ben Nejma, David Hoffman, Jennifer Lippincott-Schwartz, Wallace Marshall, Gabriel Sturm, Suliana Manley

Corresponding authors: juan.landoni@epfl.ch; suliana.manley@epfl.ch

Materials and Methods

Cell culture & live stains

Most experiments were performed in U-2 OS cells (ECACC 92022711) obtained from ECACC, which were grown in McCoy's 5A Modified Medium (Gibco) supplemented with 10% fetal bovine serum, 100 U/ml penicillin and 100 mg/ml streptomycin. Other cell types used, including Cos-7 (ECACC 87021302) and HeLa cells (Cox8a-SNAP and MIC10 KO stable lines gift from T. Stephan and S. Jakobs (*25*)) were grown in Dulbecco's modified Eagle's medium (DMEM) with similar supplementation. All cells were cultured in 5% CO_2 at 37 °C and maintained in culture for a maximum of 20 passages. They were also routinely tested for *Mycoplasma* contamination and discarded if positive.

Plasmid transfection was achieved using Lipofectamine 2000 (Invitrogen) according to manufacturer's instructions, typically 2.5 µl of lipofectamine and 500 ng of DNA per 2 ml. The plasmid details and transfected amounts can be found in Supplementary table 1. Cells were imaged 12-48 h after transfection. All fluorescent protein constructs have been previously described. mt-StayGold (pCSII-EF/mt-(n1)StayGold) and ER-StayGold (pcDNA3/er-(n2)oxStayGold(c4)v2.0) were a gift from A. Miyawaki (Addgene plasmids #185823 and #186296), TFAM-RFP was derived from pMIH-TFAM-GFP plasmid, a gift from B. Kile (Addgene plasmid #113704).

For siRNA treatments, the transfection was performed using the manufacturer's instructions of Lipofectamine RNAiMAX (Invitrogen), using 0.01-2 nmol of siRNA per ml of media and imaging cells 24-48 h after transfection. MIC10-targeted siRNA were synthesized by siPOOLs Biotech (NCBI Gene ID 440574). Other oligonucleotides were synthesized by Microsynth: siMFF (5′-CGC UGA CCU GGA ACA AGG A-dTdT-3′), FIS1 (5′-CGA GCU GGU GUC UGU GGA G-dTdT-3′), siMCU (5'-GUA ACA UAC UUC AUC ACU UAU GGA A dTdT-3').

For dye-based stainings, the following reagents were used, following manufacturers' staining instructions: Mito Mitotracker Green (ThermoFisher M7514), Mitotracker Red FM (ThermoFisher M22425), Quant-iT PicoGreen (Life Technologies P7581), SYBR™ Gold Nucleic Acid Stain (Thermo Fisher Scientific, S11494), PK Mito Orange PKMO/ abberior LIVE ORANGE (Spirochrome SC053 /abberior LVORANGE), CellLight MitoRFP (Thermo, C10601).

W303 background-derived yFT016 *Saccharomyces cerevisiae* cells expressing Su9-mKate (mitochondria) and the mt-LacO 3xNeonGreen-LacI system (nucleoids) were a gift from C. Osman and F. Thoma (*9*). Cells were grown in SCD and imaged on a in agarose pads.

Ethidium bromide treatment was performed at a concentration of 50ng/ml in growth media additionally supplemented with uridine and pyruvate over 48h, after which cells were stained and imaged. MtDNA quantification was done as described in the Image Analysis section.

Fixation and immunofluorescence

For immunofluorescence, cells were plated on 12 mm glass coverslips (Menzel) 24 h before transfections or treatments. Cells were fixed with 3.2% paraformaldehyde (PFA) and 0.1% glutaraldehyde (GA) in phosphate-buffered saline (PBS), followed by washing and storage in PBS. To quench GA autofluorescence, the samples were treated with 0.5% freshly prepared sodium borohydride ($NaBH_4$) for 7 minutes. Permeabilization and blocking were carried out using 3% bovine serum albumin (BSA) and 0.1% Triton X-100 in PBS for 45-60 minutes. Primary antibodies were incubated overnight in 1% BSA at 4°C. The samples were then washed twice for 10 minutes each with 1% BSA in PBS. Secondary antibodies were applied at room temperature for 1 hour in 1% BSA. The samples were subsequently washed twice with PBS and rinsed once with ddH_2O, then immediately mounted using ProLong Gold Antifade Mountant (P36930, Invitrogen), allowing to cure for 24 hours at room temperature in the dark. The antibodies used were dsDNA antibody (ab27156, Abcam) at a 1:250 dilution and TOM20 antibody (ab186734, Abcam) at a 1:200 dilution, Alexa Fluor 488 anti-mouse and Alexa Fluor 568 anti-rabbit (A-11011 and A32723, Invitrogen), diluted 1:400.

Light microscopy

Widefield imaging was performed on a Zeiss Axio Observer 7 inverted microscope, equipped with an sCMOS camera (Photometrics Prime), a CoolLED pE-800 LED illumination system, and a 63x 1.40 NA oil immersion objective (Zeiss Plan-Apochromat 63/1.3 Oil Ph3 M27). Volumetric yeast data was acquired on a Nikon Spinning Disk CSU W1, fast confocal, 30 z planes acquired per timepoint.

Instant structured illumination microscopy (iSIM) was performed on a custom-built microscope set-up (*51*), equipped with 488-nm and 561-nm excitation lasers, a 1.49 NA oil immersion objective (APONXOTIRF; Olympus), an sCMOS camera (PrimeBSI, 01-PRIME-BSI-R-M-16-C; Photometric), and rapid vertically scanning piezo actuated mirrors for illumination pattern homogenization. Deconvolution of the raw images was done using the Richardson Lucy algorithm implementation in the flowdec Python package (*52*) with 10 iterations. Volumetric imaging was performed using a z-step size of 200 nm.

Airyscan imaging was performed on a Zeiss LSM 980 Axio Observer inverted microscope equipped with a Colibri 5 illumination system, an Airyscan 2 detector and a 63x 1.40 NA oil inmersion objective (Zeiss Plan-Apochromat 63/1.4 Oil). Videos have a 1s frame rate for up to 360s, 40 nm pixel size, 0.65 µm pixel dwell time and 2X SR sampling. Deconvolution and reassignation of the raw data were done using the Airyscan 2D SR Standard processing on the ZEN Blue software, version 3.4.91.

Single objective light sheet imaging (SNOUTY, (*53*)) was performed using a fixed Nikon 100x 1.35 NA silicon objective (MRD73950) with 488nm and 561nm excitation lasers and ZET405/488/561/640 quad filter wheel. All imaging was performed in a stage-top environmentally controlled incubator at 37C in 8-well glass-bottom chambered cover slides (CellVis C8-1.5H-N) pre-coated with 1:100 fibronectin (Sigma, F1141). Cells were imaged at 1 volume/second (1 Hz). At 30-45 seconds the well was injected with 2 µl of 400 µM ionomycin (Thermo, I24222) for a final concentration of 4 µM in the well. Cells were then imaged for a total of 200 volumes. The 10 frames pre-pearling were selected before the injection of ionomycin, and the 10 frames after were selected once pearl morphology started to become visible.

STED imaging was performed on an Olympus IX83 equipped with an Abberior STEDYCON system and a 100x 1.45 NA oil immersion objective (Olympus UPLXAPO100XO). STED laser was a pulsed 775 nm laser with a 40 MHz repetition rate and a max power of 1.25 W, and pulse duration of 1.3 ns. The Pulsed Diode 488 and 561 lasers had a repetition rate of 40 MHz, max power of 5 mW. For both channels, excitation pulse delay was -0.2 ns and gating was set for 1ns to 6 ns. For cristae imaging, a 561 nm laser was used for excitation, and emissions were detected in the range of 575nm – 625 nm. For nucleoid imaging the excitation was with a 488 nm laser, and emissions were detected in the range of 505 nm – 550 nm. Pixel size was fixed to 30 nm x 30 nm. Pixel dwell time was 10 µs, 10 line accumulations. Pinhole was set to 0.91

AU. Frame duration was set to the minimal time allowed per field of view, resulting in frame rates as low as 3 seconds. Cristae data was deconvolved with Huygens Professional using the conservative fully automated smart template (Scientific Volume Imaging). 55 live STED acquisitions were collected across 13 separate samples (each sample was imaged up to 1h), imaged during 4 imaging sessions in separate days.

Correlative cryo-SIM/FIB-SEM

For FIB-SEM and cryo-correlative fluorescence imaging, cells were high pressure frozen to avoid the generation of fixation artifacts and to immobilize the cells rapidly enough to capture the highly transient pearled states. Cells were seeded on sapphire coverslips (3mm diameter, 50 m thickness, Nanjing Co-Energy Optical Crystal Co. Ltd, COE) prepared as described in (*54*). In brief, coverslips were washed in a basic piranha solution (5:1:1 water:ammonium hydroxide:hydrogen peroxide), washed in distilled water, sputter coated with a thin layer of gold (sputter coater Desk II, Denton Vacuum), rinsed several times in distilled water, and pre-coated with 100 µg of Matrigel (Corning) for 3 hours at 37 degrees.

U2-OS cells were seeded and allowed to grow for 18 hours, at which time cells were stained with 50 nM TMRM (ThermoFisher, T668) and SYBR Green I 10000X concentrate in DMSO (ThermoFisher S7563) at a 1:500,000 ratio for 15 minutes. Cells were then gently washed three times with 10 ml of complete medium, taking care not to flip over the coverslips. The cells were then given 15 minutes to equilibrate in 2 ml of complete medium to ensure TMRM staining was calibrated to the underlying membrane potential (membrane potential was later used to ensure the selected mitochondria were healthy and functional).

Immediately before freezing, cells were manually inspected using an inverted widefield microscope to ensure reasonable morphology and viability. Cells were then transferred to a water jacketed incubator (ThermoFisher, Midi 40) and kept at 37 °C in 5% CO2 and 100% humidity until ready for freezing. Coverslips were removed one at time from the incubator, overlaid with a 25% (w/v) solution of 40,000 MW dextran (Sigma), loaded between two hexadecane-coated freezing platelets (Technotrade International), and placed in the HPF holder. Freezing was performed using a Wohlwend Compact 2 high pressure freezer, according to the manufacturer's protocol. Frozen samples were stored under liquid nitrogen until cryo-fluorescence imaging or freeze substitution.

Cryo-fluorescence imaging of cells was performed using a custom built cryo-structured illumination microscope (SIM) as described in (*54*). Briefly, sapphire coverslips were removed from the encasing platelets under liquid nitrogen in a custom preparation chamber and loaded into a custom-designed coverslip holder, which was then transferred to the cryo-stage of the microscope using a commercial cryogenic vacuum transfer process. Following SIM image acquisition and processing, samples were returned to liquid nitrogen for storage until subsequent freeze substitution and resin embedding.

Freeze-substitution was performed with a modified version of a previously described protocol (*54*, *55*). Briefly, frozen samples were transferred to cryotubes containing freeze-substitution media (2% OsO4, 0.1% Uranyl acetate and 3% water in acetone) and placed in an automated freeze-substitution machine (AFS2, Leica Microsystems). The samples were then washed three times in anhydrous acetone and embedded in Eponate 12 (Ted Pella, Inc.). The sapphire coverslip was then removed, and the block was re-embedded in Durcapan (Sigma) resin for FIB-SEM imaging.

FIB-SEM was performed as described in (*56*). Briefly, a customized FIB-SEM using a Zeiss Capella FIB column fitted at 90 degrees on a Zeiss Merlin SEM was used to sequentially image and mill 8 nm layers from the Durcapan-embedded block. Milling steps were performed using a 15 nA gallium ion beam at 30 kV to generate two sequential 4 nm steps. Data was acquired at 500 kHz pixel−1 using a 2 nA electron beam at 1.0 kV landing energy with 8 nm xy resolution to generate isotropic voxels. Data sets were registered postacquisition using a SIFT-based algorithm.

Instance segmentations of mitochondria from 3D FIB-SEM volumes were generated by ariadne.ai. CryoSIM and FIB-SEM stacks were registered using the BigWarp Fiji plugin (*57*). In brief, multiple landmarks were selected between TMRM labeled mitochondria in SIM images and stained mitochondria in the FIB-SEM stack. Based on these landmarks, an affine transformation was used to register and fuse the SIM and FIB-SEM stacks.

Image analysis

Pearling frequency was quantified with two approaches. On one hand, events per unit of time (as in Fig. 1E and I) were manually quantified as every pearling event with an onset during the time course, regardless of their location, size or duration. To account for network and pearling size differences between treatments, a second approach was used (in Fig. 1H, 4B and 4G). Pearling probability was quantified from timelapses, as the proportion of the total mitochondrial network length which pearls within a minute of acquisition (length of pearled mitochondria during 1 minute normalized to total skeleton length at t = 0).

For two-dimensional analysis of nucleoid positioning, manually annotated 504 nm-thick smoothed line profiles along the mitochondrion were used to obtain the integrated intensities of each channel. Nucleoid centroids were identified as peaks in the nucleoid channel profile (SYBR gold or TFAM-RFP), and their distances were measured as their difference in position along the smoothed line length. Thick line profiles were similarly used to obtain the intensity data for kymographs (nucleoid distribution, splitting) and full-width half-maximum measurements (pearl and nucleoid size quantifications). Classification of pearling status was performed blinded of the nucleoid channel, ensuring the periodical pearling morphology on both the mitochondrial channel image and line profile. Modelling of random distribution was done by assigning the nucleoids on each profile random positions along the length, reordering them and recalculating the inter-nucleoid distances.

Whole-cell nucleoid quantification was performed using built-in CellProfiler 4.2.5 (*58*) functions. Briefly, nucleoid signal was segmented using three-class global Otsu thresholding (through the IdentifyPrimaryObjects module) and integrated intensity was measured by the MeasureObjectIntensity module. Nucleoids were classified from a manual mask created from the electron microscopy or mitochondrial channel data, identifying pearled regions blinded to the nucleoid signal. Mitochondrial DNA amount quantification following ethidium bromide treatment was similarly performed, segmenting mitochondria using the IdentifyPrimaryObjects module, and quantifying mean intensity of SYBR gold within the mitochondrion, to confirm specific mtDNA loss and avoid noise from nuclear dye incorporation (consequential of mtDNA loss).

For volumetric analysis of inter-nucleoid distancing, 3D iSIM images of immunolabeled mitochondrial network and DNA were processed in a custom pipeline. Shortly, mitochondrial networks were segmented and skeletonized using Nellie (*59*), obtaining labelled skeletons. Splines were then generated from branches (above 1.12 µm), using the SplineBox package (*60*) to fit cubic B-splines to the skeleton coordinates, and extended them by 300 nm to capture the entire mitochondrial length and potential tip nucleoids. Then, normal planes (1 µm wide) were computed along the splines, extracting the integrated intensity of each channel, and outputting a line profile similar to those from 2D data with distance information along the spline. The line profile, inter-nucleoid distancing and random distribution analysis was performed as above. The regular distribution values were achieved by dividing the total length of a branch between the first and last nucleoid position and dividing it by the number of nucleoids on that branch minus one.

Volumetric live SNOUTY (baseline distancing, ionomycin treatment) and Spinning disk data (yeast) were analyzed using similar approaches. The 3D skeletons of both the mitochondrial network and nucleoids were extracted using Nellie or MitoGraph (*61*). Nucleoid positions were obtained using a centroid algorithm with a minimum distance threshold, and subsequently matched/projected onto the nearest points on the

mitochondrial network skeleton. The shortest path traversal-distance algorithm was then used to calculate the inter-nucleoid distances between neighboring nucleoids.

Nucleotes (long nucleoid clusters) were defined as clusters of nucleoid signal (from SYBR gold or PicoGreen) longer than 2 µm long and stably clustered throughout the timelapse (typically > 1 min). Nucleotes were differentiated from other enlarged nucleoid formations (mito-bulbs or enlarged nucleoids (*12*, *39*, *40*)) by their maintaining mitochondrial tubular integrity.

Western blotting

Immunoblotting was done on cells following identical and parallel siRNA treatments as imaging experiments. The cell pellets were lysed in RIPA buffer (Sigma) supplemented with freshly added protease inhibitors (Sigma Aldrich 11836170001) on ice for 30 minutes. Following lysis, the lysates were centrifuged at 16,000xg for 10 minutes at 4 °C to separate the insoluble material. Protein concentrations were quantified using the Pierce BCA protein assay kit (Life Technologies, 23227), and equal protein amounts (30–50 µg per lane) were resolved on self-cast 7.5% or 15% SDS–PAGE gels. For immunoblotting, proteins were transferred onto nitrocellulose membranes (BioRad) via electrophoresis and probed with the appropriate primary antibodies, which were diluted in 5% non-fat dry milk in Tris-buffered saline with Tween 20 (TBST). The blots were then incubated with anti-rabbit or anti-mouse horseradish peroxidase (HRP)-conjugated secondary antibodies (GE Healthcare) and visualized using ECL (GE Healthcare). The antibodies used were against: MIC10 (Abcam, ab84969, kind gift from Veronica Eisner) diluted 1:1000, FIS1 (LuBioScience GmbH, 10956-1-AP), diluted 1:2000, MFF (Life Technologies, PA5-67357), diluted 1:1000), MCU (Abcam, ab219827) tubulin (Abcam, ab18251), diluted 1:2000. Densitometry was performed using FIJI ImageJ software. Uncropped western blots can be found in Fig. S3.

Experimental and statistical design

Statistical analyses and plotting were performed in R version 4.2.2 within the Visual Studio Code environment version 1.93.0. No statistical method was used to predetermine sample size. Only technically failed data were excluded from the analysis and partial blinding and automation was applied whenever possible to minimize observer bias (e.g. choice and classification of pearling regions using mitochondrial markers blinded to the nucleoid channel, and automatic quantification of inter-nucleoid distances blinded to genotype).

When reasonable, all data points are clearly displayed in data visualization and represent separate biological measurements (typically individual cells), overlayed on boxplots representing the median, two quartiles (Q2 and Q3), and minima and maxima as central line, box bounds and whiskers respectively. Outliers are defined as being beyond 1.5 times the interquartile range. Statistical tests were performed on relevant biological units (e.g. median per cell instead of each inter-nucleoid distance separately) to avoid non-informative inflated significance.

Movie S1.

iSIM time-lapse of a U2-OS cell mitochondrion undergoing consecutive reversible pearling, and eventually fission. Mitochondrial matrix labeled with mt-StayGold. Arrowheads and inset highlight pearling events, and empty arrowheads indicate fission events.

Movie S2.

Live STED timelapse of mitochondrial inner membrane (PKMO, green) and nucleoid (SYBR gold, pink) during spontaneous pearling in a U2-OS cell. Pink arrowheads indicate nucleoid foci and green arrowheads lamellar cristae.

Movie S3.

Timelapses of mitochondrial inner membrane (PKMO, green) and nucleoid (PicoGreen, pink) during spontaneous pearling in MIC10-deficient HeLa cells. Empty arrowheads indicate nucleoid-free mitochondria, filled arrowheads pearling events (reversible in pink, persistent in green) and rounded pink arrowheads mark nucleote aggregates.

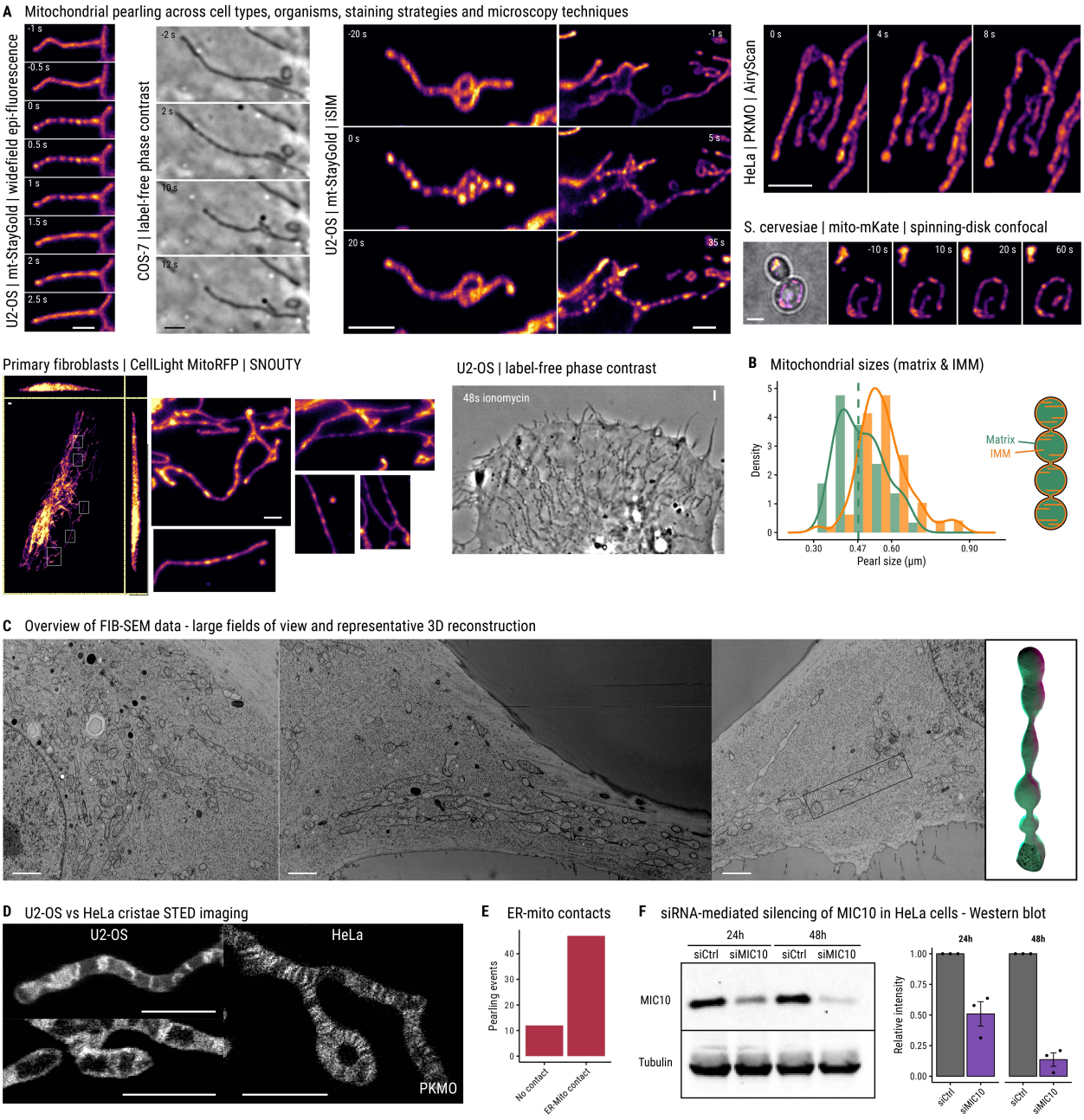

Fig. S1.

(A) Montage of spontaneous pearling in a variety of models, contrasting methods and microscopy techniques. Left-to-right top-to-bottom: Osteosarcoma U2-OS cell, widefield epi-fluorescent microscopy, genetically encoded protein mt-StayGold; African green monkey kidney fibroblast-like COS-7 cell, label-free phase contrast microscopy; U2-OS cell, iSIM, mt-StayGold; HeLa cell, AiryScan, PKMO dye; S. cerevisiae cell, Spinning disk confocal, mt-mKate; Primary fibroblast cell, SNOUTY, CellLight MitoRFP; U2-OS cell under ionomycin treatment, label-free phase-contrast microscopy. **(B)** Distribution of pearl sizes (FWHM) as measured from matrix-targeted mt-StayGold on iSIM or IMM-targeted PKMO on STED. Dashed line indicates median value, graphical depiction of different mitochondrial compartments on the right. **(C)** Large fields of view of FIB-SEM in U2-OS cells, 3D reconstruction of a pearled mitochondrion on the right. **(D)** STED imaging of mitochondrial cristae (stained by PKMO) of wildtype U2-OS and HeLa cells. **(E)**

Quantification of spontaneous pearling with or without clear ER-StayGold proximity (as in Figure 1E). **(F)** Immunoblot of MIC10 siRNA efficiency and quantification, three repeats. All error bars represent 2 µm.

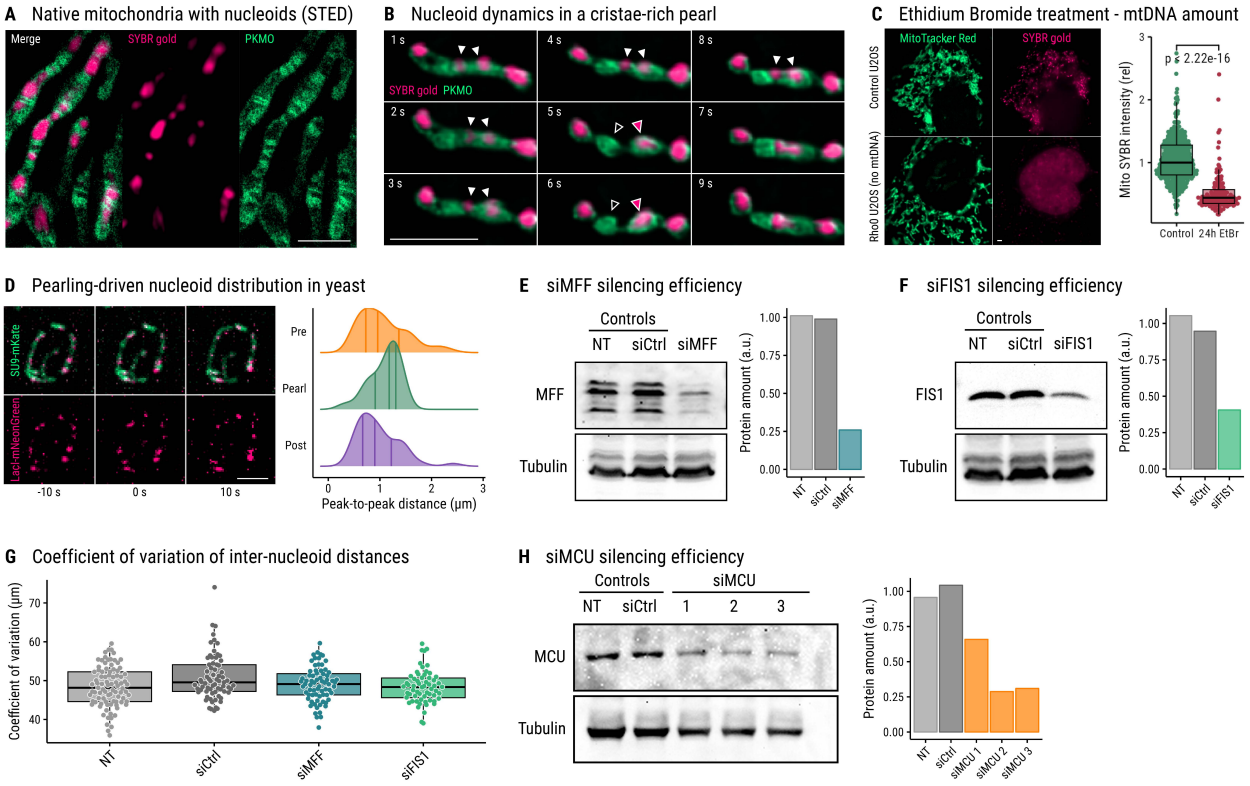

Fig. S2.

(A) Live STED imaging of mitochondria and nucleoids (stained with PKMO and SYBR gold respectively. **(B)** STED timelapse of spontaneous pearling as in (A). **(C)** Quantification of mtDNA amount in ethidium bromide experiment, representative images on the right and quantification of mean SYBR gold intensity within segmented mitochondria relative to controls on the right. Stronger nuclear staining in treated cells is an expected consequence of mtDNA loss. P value from two-sided Wilcoxon test. **(D)** Analysis of nucleoid distribution during spontaneous pearling in yeast: representative pearling event on the left, inter-nucleoid distancing distribution during and 15 s before and after. **(E-F)** Silencing efficiency of siRNA targeting MFF (E) and FIS1 (F), along with their densitometric quantification. **(G)** Coefficient of variation of 3D inter-nucleoid distances per cell in siRNA-treated cells. **(H)** Silencing efficiency of siRNA targeting MCU, along with its densitometric quantification. Three siMCU sequences were tested, of which number 2 was selected for further experimentation. All error bars represent 2 µm.

Supplementary Figure S3: Uncropped western blots

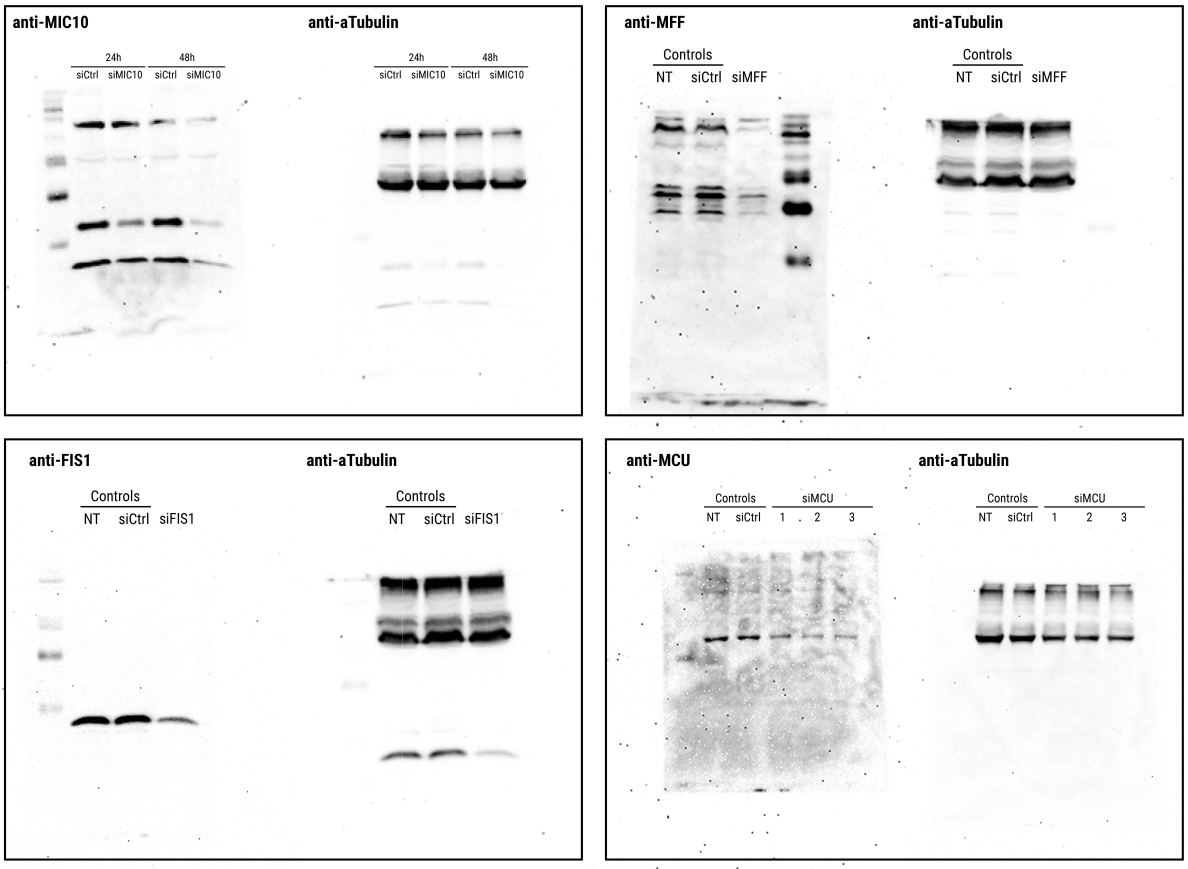

Fig. S3.

Uncropped western blots depicted in Fig. S1-2, along with their loading controls.

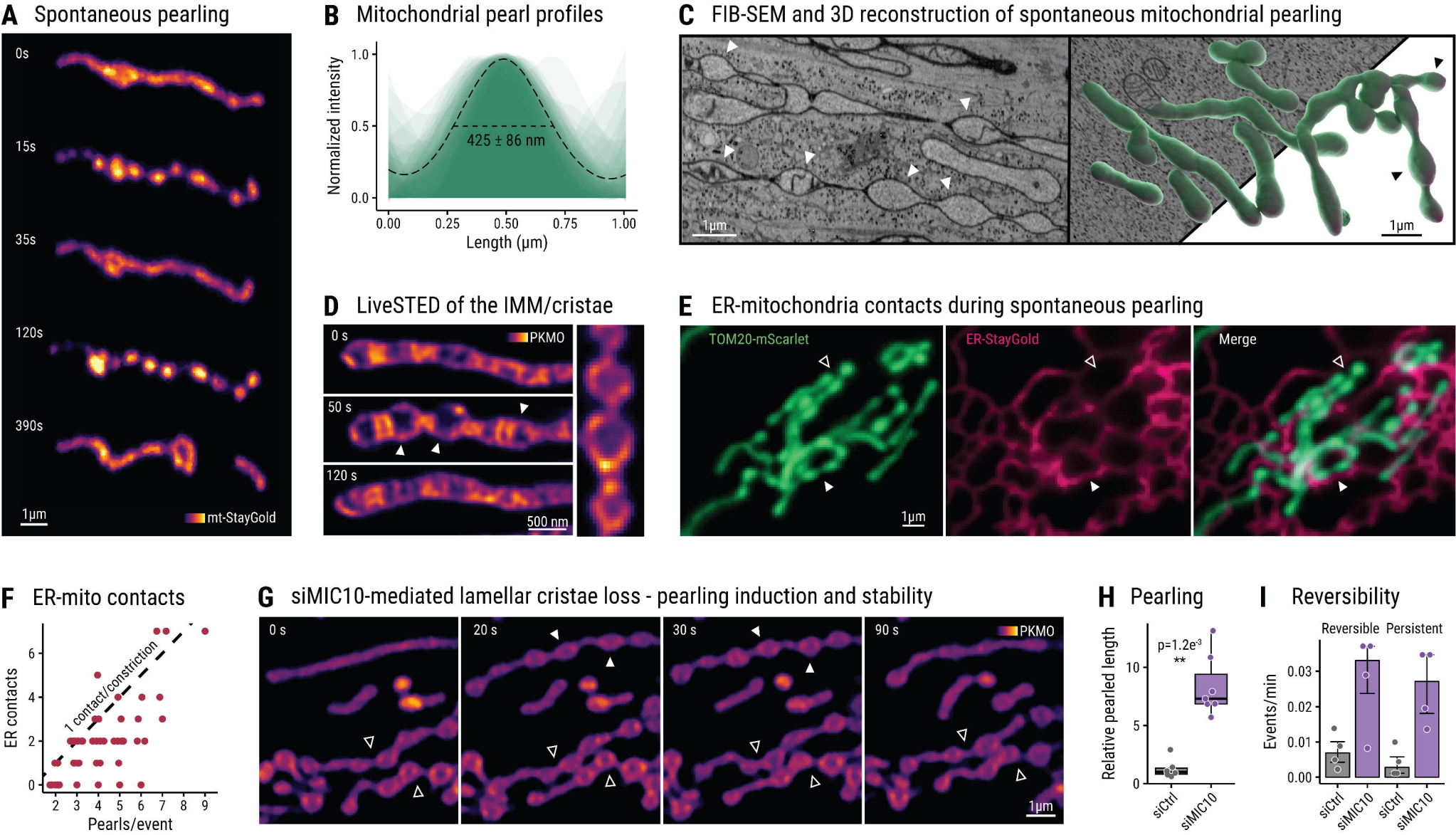
A Spontaneous pearling
0s
15s
35s
120s
390s
1µm
mt-StayGold
B Mitochondrial pearl profiles
Normalized intensity
1.0
0.5
0.0
425 ± 86 nm
0.00
0.25
0.50
0.75
1.00
Length (µm)
C FIB-SEM and 3D reconstruction of spontaneous mitochondrial pearling
1µm
1µm
D LiveSTED of the IMM/cristae
0 s
PKMO
50 s
120 s
500 nm
E ER-mitochondria contacts during spontaneous pearling
TOM20-mScarlet
ER-StayGold
Merge
1µm
F ER-mito contacts
ER contacts
1 contact/constriction
Pearls/event
G siMIC10-mediated lamellar cristae loss - pearling induction and stability
0 s
20 s
30 s
90 s
PKMO
1µm
H Pearling
Relative pearled length
p=1.2e-3
**
siCtrl
siMIC10
I Reversibility
Reversible
Persistent
Events/min
siCtrl
siMIC10
siCtrl
siMIC10

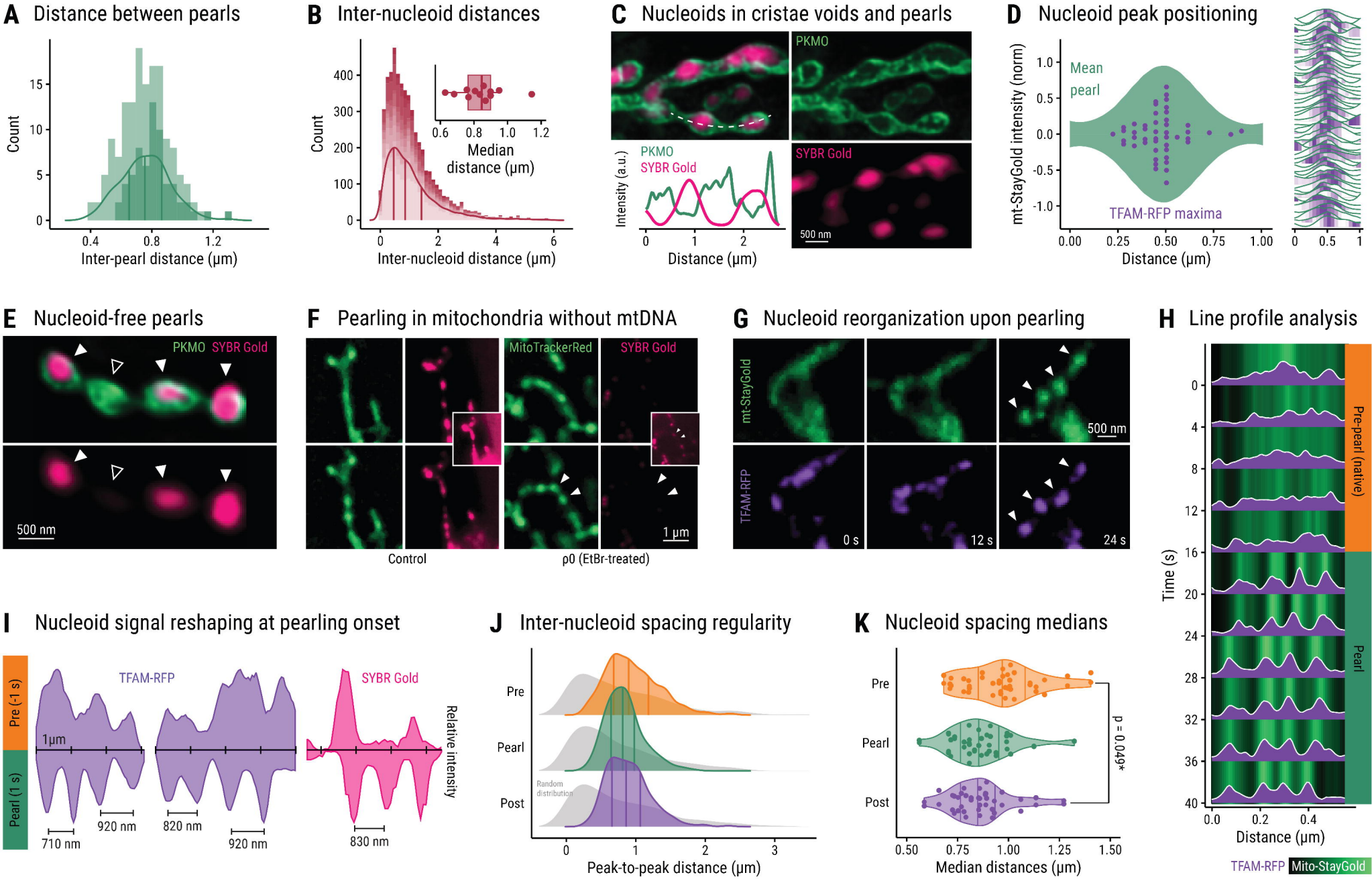
A Distance between pearls
Count
Inter-pearl distance (µm)
B Inter-nucleoid distances
Count
Median distance (µm)
Inter-nucleoid distance (µm)
C Nucleoids in cristae voids and pearls
PKMO
PKMO
SYBR Gold
Intensity (a.u.)
Distance (µm)
SYBR Gold
500 nm
D Nucleoid peak positioning
mt-StayGold intensity (norm)
Mean pearl
TFAM-RFP maxima
Distance (µm)
E Nucleoid-free pearls
PKMO SYBR Gold
500 nm
F Pearling in mitochondria without mtDNA
MitoTrackerRed
SYBR Gold
1 µm
Control
ρ0 (EtBr-treated)
G Nucleoid reorganization upon pearling
mt-StayGold
TFAM-RFP
500 nm
0 s
12 s
24 s
H Line profile analysis
Time (s)
Pre-pearl (native)
Pearl
Distance (µm)
TFAM-RFP Mito-StayGold
I Nucleoid signal reshaping at pearling onset
Pre (-1 s)
Pearl (1 s)
TFAM-RFP
SYBR Gold
1µm
710 nm
920 nm
820 nm
920 nm
830 nm
Relative intensity
J Inter-nucleoid spacing regularity
Pre
Pearl
Post
Random distribution
Peak-to-peak distance (µm)
K Nucleoid spacing medians
Pre
Pearl
Post
p = 0.049*
Median distances (µm)

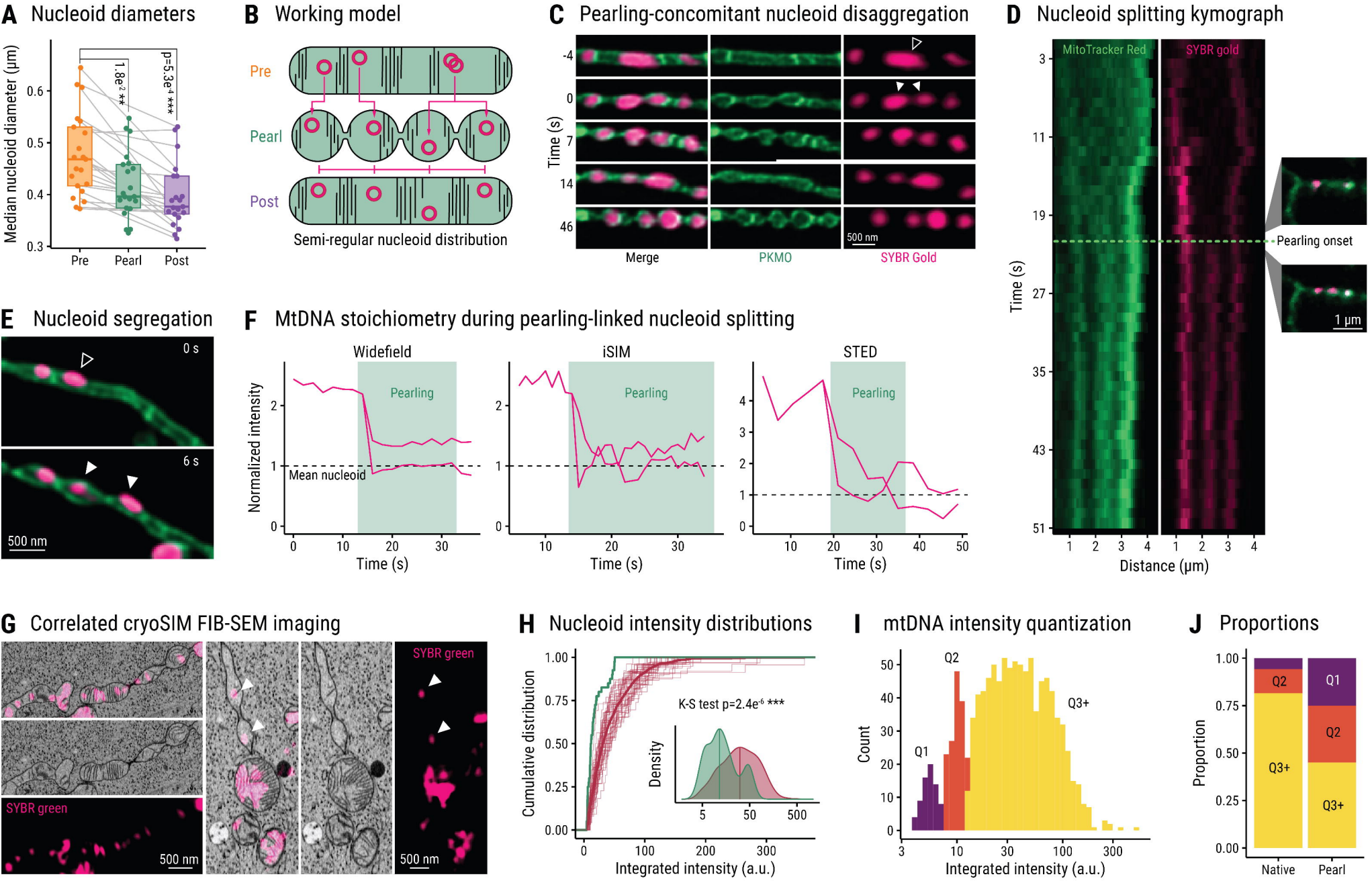
A Nucleoid diameters
Median nucleoid diameter (µm)
0.6
0.5
0.4
0.3
Pre
Pearl
Post
1.8e-2 **
p=5.3e-4 ***
B Working model
Pre
Pearl
Post
Semi-regular nucleoid distribution
C Pearling-concomitant nucleoid disaggregation
Time (s)
-4
0
7
14
46
500 nm
Merge
PKMO
SYBR Gold
D Nucleoid splitting kymograph
MitoTracker Red
SYBR gold
Time (s)
3
11
19
27
35
43
51
Pearling onset
1 µm
Distance (µm)
E Nucleoid segregation
0 s
6 s
500 nm
F MtDNA stoichiometry during pearling-linked nucleoid splitting
Widefield
iSIM
STED
Normalized intensity
Pearling
Mean nucleoid
Time (s)
G Correlated cryoSIM FIB-SEM imaging
SYBR green
500 nm
H Nucleoid intensity distributions
Cumulative distribution
K-S test p=2.4e-6 ***
Density
Integrated intensity (a.u.)
I mtDNA intensity quantization
Count
Q1
Q2
Q3+
Integrated intensity (a.u.)
J Proportions
Proportion
Q1
Q2
Q3+
Native
Pearl

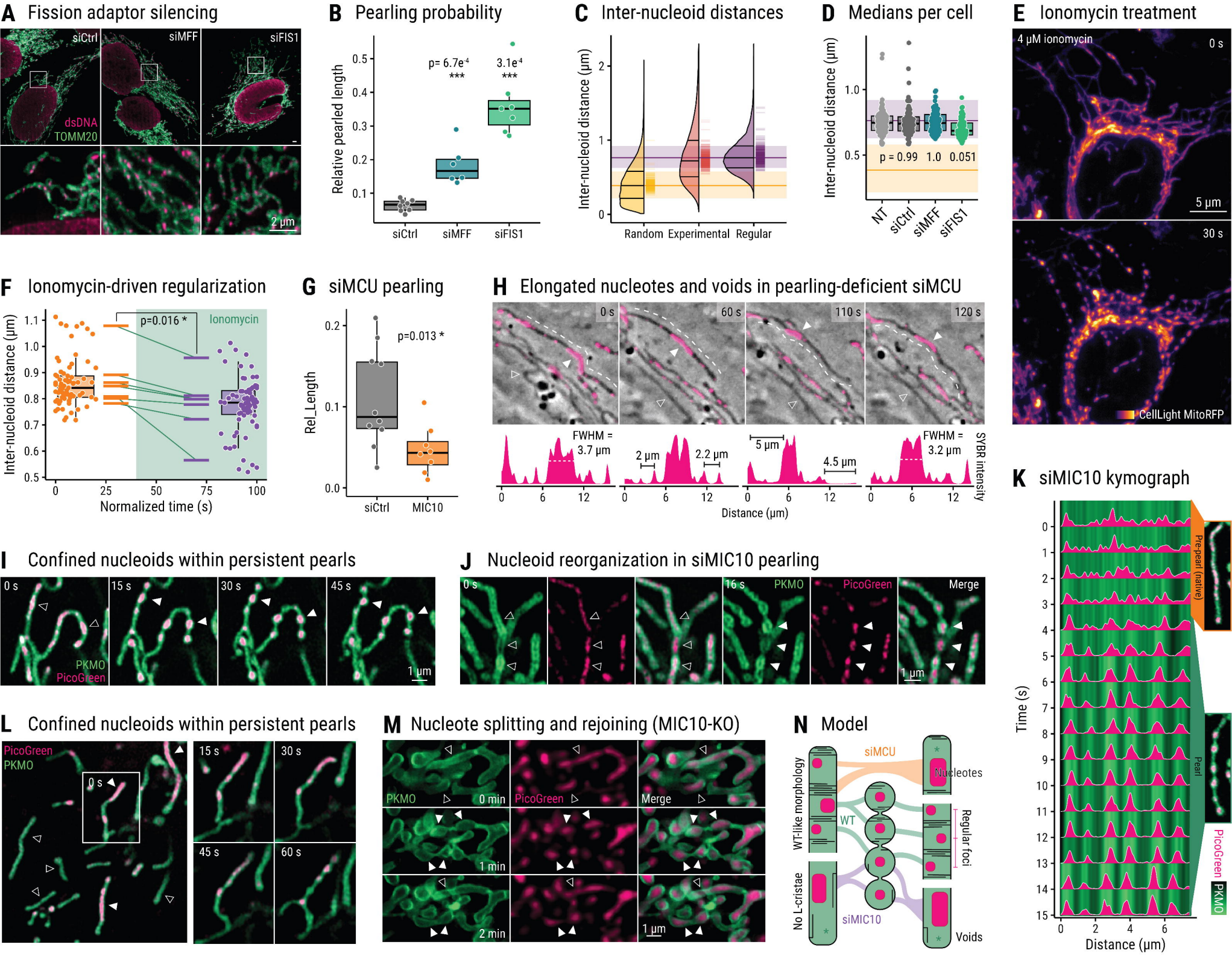
A Fission adaptor silencing
siCtrl
siMFF
siFIS1
dsDNA
TOMM20
2 µm
B Pearling probability
Relative pearled length
p= 6.7e-4
***
3.1e-4
***
siCtrl
siMFF
siFIS1
C Inter-nucleoid distances
Inter-nucleoid distance (µm)
Random
Experimental
Regular
D Medians per cell
Inter-nucleoid distance (µm)
p = 0.99
1.0
0.051
NT
siCtrl
siMFF
siFIS1
E Ionomycin treatment
4 µM ionomycin
0 s
5 µm
30 s
CellLight MitoRFP
F Ionomycin-driven regularization
p=0.016 *
Ionomycin
Inter-nucleoid distance (µm)
Normalized time (s)
G siMCU pearling
p=0.013 *
Rel_Length
siCtrl
MIC10
H Elongated nucleotes and voids in pearling-deficient siMCU
0 s
60 s
110 s
120 s
FWHM = 3.7 µm
2 µm
2.2 µm
5 µm
4.5 µm
FWHM = 3.2 µm
SYBR intensity
Distance (µm)
I Confined nucleoids within persistent pearls
0 s
15 s
30 s
45 s
PKMO
PicoGreen
1 µm
J Nucleoid reorganization in siMIC10 pearling
0 s
16 s
PKMO
PicoGreen
Merge
1 µm
K siMIC10 kymograph
Time (s)
Pre-pearl (native)
Pearl
PicoGreen
PKMO
Distance (µm)
L Confined nucleoids within persistent pearls
PicoGreen
PKMO
0 s
15 s
30 s
45 s
60 s
M Nucleote splitting and rejoining (MIC10-KO)
PKMO
0 min
PicoGreen
Merge
1 min
2 min
1 µm
N Model
siMCU
Nucleotes
WT-like morphology
WT
Regular foci
No L-cristae
siMIC10
Voids